J. Fluid Mech. (2024), *vol*. 984, A35, doi:10.1017/jfm.2024.220

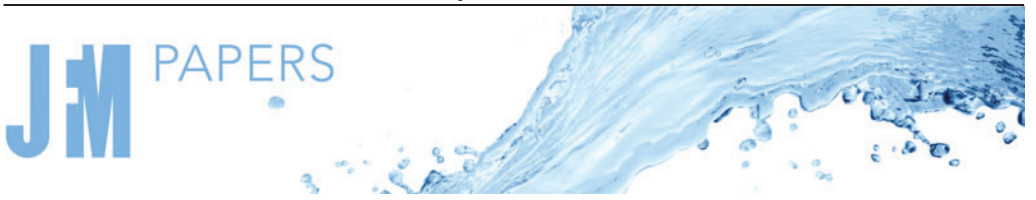

Scale-by-scale non-equilibrium with Kolmogorov-like scalings in non-homogeneous stationary turbulence

P. Beaumard[1], P. Bragança[1], C. Cuvier[1], K. Steiros[2] and J.C. Vassilicos[1],†

[1]Univ. Lille, CNRS, ONERA, Arts et Metiers Institute of Technology, Centrale Lille, UMR 9014, LMFL – Laboratoire de Mécanique des Fluides de Lille, Kampé de Fériet, F-59000 Lille, France

[2]Department of Aeronautics, Imperial College London, London SW7 2AZ, UK

(Received 13 June 2023; revised 19 January 2024; accepted 24 February 2024)

An improved version of the non-equilibrium theory of non-homogeneous turbulence of Chen & Vassilicos (*J. Fluid Mech.*, vol. 938, 2022, A7) predicts that an intermediate range of length scales exists where the interscale turbulence transfer rate, the two-point interspace turbulence transport rate and the two-point pressure gradient velocity correlation term in the two-point small-scale turbulent energy equation are all proportional to the turbulence dissipation rate and independent of length scale. Particle image velocimetry measurements in a field of view under the turbulence-generating impellers in a baffled water tank support these predictions and show that the measured small-scale turbulence is significantly non-homogeneous. The particle image velocimetry measurements also suggest that the rate with which large scales lose energy to the small scales in the two-point large-scale turbulent energy equation also appears to be approximately proportional to the turbulence dissipation rate and independent of length scale in the same intermediate range and that this rate may not balance the interscale turbulence transfer rate in the two-point small-scale turbulent energy equation because of turbulent energy transport caused by the non-homogeneity.

Key words: turbulence theory

1. Introduction

The Kolmogorov 1941 theory of statistically homogeneous turbulence (see Frisch 1995; Pope 2000) predicts that the interscale transfer rate of turbulent kinetic energy is approximately balanced by the turbulence dissipation rate across a wide range of inertial range length scales as the Reynolds number tends to infinity. This prediction of

† Email address for correspondence: john-christos.vassilicos@cnrs.fr

scale-by-scale equilibrium (the word equilibrium in this paper is not used in the sense reserved in statistical physics for stationary states satisfying detailed balance such as thermal equilibria) holds for statistically stationary forced homogeneous turbulence (see Frisch 1995) but is also made for decaying homogeneous turbulence on the basis of a small-scale stationarity hypothesis (see Frisch (1995), Pope (2000) and § 2 of Chen & Vassilicos (2022)). A widely held view is that the turbulence is always statistically homogeneous at small enough length scales if the Reynolds number is large enough. But what if the Reynolds number, even if high, is not high enough for homogeneity to exist at the smallest scales? And if, in such circumstances, one finds simple scalings and scale-by-scale balances which appear independent of the details of the non-homogeneity, would these non-homogeneity laws survive as the Reynolds number is taken to infinity? Or would they locally tend to Kolmogorov scale-by-scale equilibrium, in which case Kolmogorov scale-by-scale equilibrium would, in some sense, be an asymptotic case of these non-homogeneity laws?

In this paper we address statistically stationary non-homogeneous turbulence at moderate to high Reynolds numbers and we attempt to provide some partial answer to the first one of these questions: can simple scale-by-scale turbulence energy balances exist in non-homogeneous turbulence? The questions concerning the limit towards infinite Reynolds numbers cannot be answered at present and may, perhaps, never be answered unless one can some day answer them by rigorous mathematical analysis of the Navier–Stokes equations. The problem with claims made for Reynolds numbers tending to infinity is that one can always argue that the Reynolds number is not large enough if an experiment or simulation does not confirm the claims.

We chose to study the turbulent flow under turbulence-generating rotating impellers in a baffled tank where the baffles break the rotation of the flow. This is a flow where the turbulence is statistically stationary, where Taylor length-based Reynolds numbers up to order 10^3 can be achieved, where different types of impeller can produce significantly different turbulent flows and where we can use a two-dimensional two-component (2D2C) particle image velocimetry (PIV) that is highly resolved in space and capable of accessing estimates of turbulence dissipation rates as well as parts of various interscale and interspace turbulent transfer/transport rates. Only full three-dimensional three-component highly resolved PIV measurements can, in principle, access the turbulence dissipation and these transfer/transport rates in full, but such an approach is currently beyond our reach over the significant range of length scales needed to establish scale-by-scale energy balances. The truncated transfer/transport rates obtained by our 2D2C PIV do, nevertheless, exhibit interesting properties, in particular because they are concordant with a recent non-equilibrium theory of non-homogeneous turbulence (Chen & Vassilicos 2022) which we also further develop here.

In the following section we present the two-point scale-by-scale equations which form the basis of this study's theoretical framework. In § 3, we discuss interscale turbulent energy transfers and the special case of freely decaying statistically homogeneous turbulence as a point of reference. Section 4 presents the experimental apparatus and the 2D2C PIV. We use our PIV measurements to assess two-point turbulence production in § 5 and linear transport terms (e.g. mean advection) in § 6. In § 7 we present intermediate similarity predictions and PIV measurements of second-order structure functions of turbulent fluctuating velocities. Section 8 presents theoretical predictions of non-equilibrium small-scale turbulent energy budgets for non-homogeneous turbulence and related 2D2C PIV measurements. Finally, § 9 presents measurements and a theoretical discussion of elements of the large-scale turbulent energy budget, § 10 proposes a small-scale homogeneity hypothesis and we conclude in § 11.

2. Theoretical framework based on two-point Navier–Stokes equations

Interscale turbulence transfers for incompressible turbulence can be studied in the presence of all other co-existing turbulence transfer/transport mechanisms in terms of two-point equations exactly derived from the incompressible Navier–Stokes equations (see Hill 2001, 2002; Germano 2007) without any hypotheses or assumptions, in particular no assumptions of homogeneity or periodicity. The incompressible Navier–Stokes equation is written at two points $\boldsymbol{\zeta}^- = \boldsymbol{X} - \boldsymbol{r}$ and $\boldsymbol{\zeta}^+ = \boldsymbol{X} + \boldsymbol{r}$ in physical space (see figure 1), where $\boldsymbol{X}$ is the centroid and $\boldsymbol{2r}$ is the two-point separation vector. One defines the two-point velocity half-difference $\boldsymbol{\delta u}(\boldsymbol{X}, \boldsymbol{r}, t) \equiv (\boldsymbol{u}^+ - \boldsymbol{u}^-)/2$, where $\boldsymbol{u}^+ \equiv \boldsymbol{u}(\boldsymbol{\zeta}^+)$ and $\boldsymbol{u}^- \equiv \boldsymbol{u}(\boldsymbol{\zeta}^-)$ are the fluid velocities at each of the two points, and the two-point pressure half-difference $\delta p(\boldsymbol{X}, \boldsymbol{r}, t) \equiv (p^+ - p^-)/2$, where $p^+ \equiv p(\boldsymbol{\zeta}^+)$ and $p^- \equiv p(\boldsymbol{\zeta}^-)$ are the pressure over density ratios at each of the two points. Incompressibility immediately imposes $\nabla_X \cdot \boldsymbol{\delta u} = \nabla_r \cdot \boldsymbol{\delta u} = 0$ and the Navier–Stokes equation implies (Hill 2001, 2002)

$$\frac{\partial \boldsymbol{\delta u}}{\partial t} + (\boldsymbol{u}_X \cdot \nabla_X)\,\boldsymbol{\delta u} + (\boldsymbol{\delta u} \cdot \nabla_r)\,\boldsymbol{\delta u} = -\nabla_X \delta p + \frac{\nu}{2}\nabla_X{}^2 \boldsymbol{\delta u} + \frac{\nu}{2}\nabla_r{}^2 \boldsymbol{\delta u}, \tag{2.1}$$

where $\boldsymbol{u}_X(\boldsymbol{X}, \boldsymbol{r}, t) \equiv (\boldsymbol{u}^+ + \boldsymbol{u}^-)/2$; ∇_X and $\nabla_X{}^2$ are the gradient and Laplacian in $\boldsymbol{X}$ space; ∇_r and $\nabla_r{}^2$ are the gradient and Laplacian in $\boldsymbol{r}$ space; and ν is the kinematic viscosity.

An energy equation is readily obtained by multiplying (2.1) with $2\boldsymbol{\delta u}$:

$$\begin{aligned}&\frac{\partial |\boldsymbol{\delta u}|^2}{\partial t} + \nabla_X \cdot (\boldsymbol{u}_X |\boldsymbol{\delta u}|^2) + \nabla_r \cdot (\boldsymbol{\delta u} |\boldsymbol{\delta u}|^2) \\ &\quad = -2\nabla_X \cdot (\boldsymbol{\delta u}\delta p) + \frac{\nu}{2}\nabla_X{}^2 |\boldsymbol{\delta u}|^2 + \frac{\nu}{2}\nabla_r{}^2 |\boldsymbol{\delta u}|^2 - \frac{1}{2}\epsilon^+ - \frac{1}{2}\epsilon^-,\end{aligned} \tag{2.2}$$

where $\epsilon^+ = \nu(\partial u_i^+/\partial \zeta_k^+)(\partial u_i^+/\partial \zeta_k^+)$ and $\epsilon^- = \nu(\partial u_i^-/\partial \zeta_k^-)(\partial u_i^-/\partial \zeta_k^-)$. With a Reynolds decomposition $\boldsymbol{\delta u} = \overline{\boldsymbol{\delta u}} + \boldsymbol{\delta u}'$, $\boldsymbol{u}_X = \overline{\boldsymbol{u}_X} + \boldsymbol{u}_X{}'$, $\delta p = \delta \bar{p} + \delta p'$ where the overline signifies an average over time under the assumption of statistical stationarity, this general two-point energy equation leads to the following pair of two-point energy equations:

$$\begin{aligned}&(\overline{\boldsymbol{u}_X} \cdot \nabla_X + \boldsymbol{\delta \bar{u}} \cdot \nabla_r)\,\frac{1}{2}|\boldsymbol{\delta \bar{u}}|^2 + P_r + P_{Xr}^s + \frac{\partial}{\partial x_j}(\delta \overline{u_i} \overline{u_{Xj}' \delta u_i'}) + \frac{\partial}{\partial r_j}(\delta \overline{u_i} \overline{\delta u_j' \delta u_i'}) \\ &\quad = -\nabla_X \cdot (\boldsymbol{\delta \bar{u}} \delta \bar{p}) + \frac{\nu}{2}\nabla_X{}^2 \frac{1}{2}|\boldsymbol{\delta \bar{u}}|^2 + \frac{\nu}{2}\nabla_r{}^2 \frac{1}{2}|\boldsymbol{\delta \bar{u}}|^2 - \frac{\nu}{4}\frac{\partial \bar{u}_i^+}{\partial \zeta_k^+}\frac{\partial \bar{u}_i^+}{\partial \zeta_k^+} - \frac{\nu}{4}\frac{\partial \bar{u}_i^-}{\partial \zeta_k^-}\frac{\partial \bar{u}_i^-}{\partial \zeta_k^-},\end{aligned} \tag{2.3}$$

$$\begin{aligned}&(\overline{\boldsymbol{u}_X} \cdot \nabla_X + \boldsymbol{\delta \bar{u}} \cdot \nabla_r)\,\frac{1}{2}\overline{|\boldsymbol{\delta u}'|^2} - P_r - P_{Xr}^s + \nabla_X \cdot \left(\overline{\boldsymbol{u}_X{}' \frac{1}{2}|\boldsymbol{\delta u}'|^2}\right) + \nabla_r \cdot \left(\overline{\boldsymbol{\delta u}' \frac{1}{2}|\boldsymbol{\delta u}'|^2}\right) \\ &\quad = -\nabla_X \cdot \overline{(\boldsymbol{\delta u}' \delta p')} + \frac{\nu}{2}\nabla_X{}^2 \frac{1}{2}\overline{|\boldsymbol{\delta u}'|^2} + \frac{\nu}{2}\nabla_r{}^2 \frac{1}{2}\overline{|\boldsymbol{\delta u}'|^2} - \frac{\nu}{4}\overline{\frac{\partial u_i'^+}{\partial \zeta_k^+}\frac{\partial u_i'^+}{\partial \zeta_k^+}} - \frac{\nu}{4}\overline{\frac{\partial u_i'^-}{\partial \zeta_k^-}\frac{\partial u_i'^-}{\partial \zeta_k^-}},\end{aligned} \tag{2.4}$$

where $P_r = -\overline{\delta u_j' \delta u_i'}\frac{\partial \delta \overline{u_i}}{\partial r_j} = -\overline{\delta u_j' \delta u_i'}\frac{1}{2}[\Sigma_{ij}(\boldsymbol{X} + \boldsymbol{r}) + \Sigma_{ij}(\boldsymbol{X} - \boldsymbol{r})]$ and $P_{Xr}^s = -\overline{u_{Xj}' \delta u_i'}(\partial \delta \overline{u_i}/\partial X_j)$, with $\Sigma_{ij} \equiv \frac{1}{2}(\partial \overline{u_i}/\partial X_j + \partial \overline{u_j}/\partial X_i)$, are two-point turbulence production rates. Indeed, being proportional to mean flow gradient terms and to averages of products

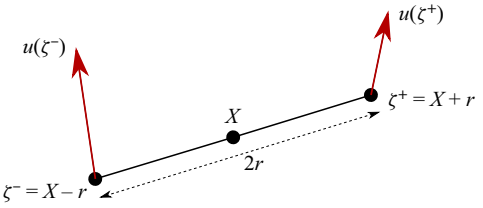

Figure 1. Schematic of fluid velocities at points $\boldsymbol{\zeta}^- = \boldsymbol{X} - \boldsymbol{r}$ and $\boldsymbol{\zeta}^+ = \boldsymbol{X} + \boldsymbol{r}$.

of fluctuating velocities, they represent linear turbulence fluctuation processes and they exchange energy between $|\boldsymbol{\delta}\bar{\boldsymbol{u}}|^2$ and $\overline{|\boldsymbol{\delta u'}|^2}$ because they appear with opposite signs in (2.3) and (2.4) as already noted by Alves Portela, Papadakis & Vassilicos (2017).

A complete two-point description also requires the evolution equation for the two-point velocity half-sum $\boldsymbol{u}_{\boldsymbol{X}}(\boldsymbol{X}, \boldsymbol{r}, t)$. This equation was first obtained by Germano (2007):

$$\frac{\partial \boldsymbol{u}_{\boldsymbol{X}}}{\partial t} + (\boldsymbol{u}_{\boldsymbol{X}} \cdot \nabla_{\boldsymbol{X}})\, \boldsymbol{u}_{\boldsymbol{X}} + (\boldsymbol{\delta u} \cdot \nabla_{\boldsymbol{r}})\, \boldsymbol{u}_{\boldsymbol{X}} = -\nabla_{\boldsymbol{X}} p_{\boldsymbol{X}} + \frac{\nu}{2} \nabla_{\boldsymbol{X}}{}^2 \boldsymbol{u}_{\boldsymbol{X}} + \frac{\nu}{2} \nabla_{\boldsymbol{r}}{}^2 \boldsymbol{u}_{\boldsymbol{X}}, \tag{2.5}$$

where $p_{\boldsymbol{X}} \equiv (p^+ + p^-)/2$, and note that $\boldsymbol{u}_{\boldsymbol{X}}$ is incompressible, i.e. $\nabla_{\boldsymbol{X}} \cdot \boldsymbol{u}_{\boldsymbol{X}} = \nabla_{\boldsymbol{r}} \cdot \boldsymbol{u}_{\boldsymbol{X}} = 0$. An energy equation, also first derived by Germano (2007), is readily obtained by multiplying (2.5) with $2\boldsymbol{u}_{\boldsymbol{X}}$:

$$\frac{\partial |\boldsymbol{u}_{\boldsymbol{X}}|^2}{\partial t} + \nabla_{\boldsymbol{X}} \cdot (\boldsymbol{u}_{\boldsymbol{X}} |\boldsymbol{u}_{\boldsymbol{X}}|^2) + \nabla_{\boldsymbol{r}} \cdot (\boldsymbol{\delta u} |\boldsymbol{u}_{\boldsymbol{X}}|^2) = -2\nabla_{\boldsymbol{X}} \cdot (\boldsymbol{u}_{\boldsymbol{X}} p_{\boldsymbol{X}}) + \frac{\nu}{2} \nabla_{\boldsymbol{X}}{}^2 |\boldsymbol{u}_{\boldsymbol{X}}|^2 + \frac{\nu}{2} \nabla_{\boldsymbol{r}}{}^2 |\boldsymbol{u}_{\boldsymbol{X}}|^2 - \frac{1}{2}\epsilon^+ - \frac{1}{2}\epsilon^-. \tag{2.6}$$

A pair of Reynolds-averaged two-point energy equations follows (using $p_{\boldsymbol{X}} = \overline{p_{\boldsymbol{X}}} + p'_{\boldsymbol{X}}$):

$$(\overline{\boldsymbol{u}_{\boldsymbol{X}}} \cdot \nabla_{\boldsymbol{X}} + \boldsymbol{\delta}\bar{\boldsymbol{u}} \cdot \nabla_{\boldsymbol{r}}) \frac{1}{2} |\overline{\boldsymbol{u}_{\boldsymbol{X}}}|^2 + P_{\boldsymbol{X}} + P^l_{\boldsymbol{X}r} + \frac{\partial}{\partial x_j} (\overline{u_{\boldsymbol{X}i}} \overline{u'_{\boldsymbol{X}i} u'_{\boldsymbol{X}j}}) + \frac{\partial}{\partial r_j} (\overline{u_{\boldsymbol{X}i}} \overline{\delta u'_j u'_{\boldsymbol{X}i}})$$
$$= -\nabla_{\boldsymbol{X}} \cdot (\overline{\boldsymbol{u}_{\boldsymbol{X}} p_{\boldsymbol{X}}}) + \frac{\nu}{2} \nabla_{\boldsymbol{X}}{}^2 \frac{1}{2} |\overline{\boldsymbol{u}_{\boldsymbol{X}}}|^2 + \frac{\nu}{2} \nabla_{\boldsymbol{r}}{}^2 \frac{1}{2} |\overline{\boldsymbol{u}_{\boldsymbol{X}}}|^2 - \frac{\nu}{4} \frac{\partial \bar{u}_i^+}{\partial \zeta_k^+} \frac{\partial \bar{u}_i^+}{\partial \zeta_k^+} - \frac{\nu}{4} \frac{\partial \bar{u}_i^-}{\partial \zeta_k^-} \frac{\partial \bar{u}_i^-}{\partial \zeta_k^-}, \tag{2.7}$$

$$(\overline{\boldsymbol{u}_{\boldsymbol{X}}} \cdot \nabla_{\boldsymbol{X}} + \boldsymbol{\delta}\bar{\boldsymbol{u}} \cdot \nabla_{\boldsymbol{r}}) \frac{1}{2} \overline{|\boldsymbol{u}_{\boldsymbol{X}}'|^2} - P_{\boldsymbol{X}} - P^l_{\boldsymbol{X}r} + \nabla_{\boldsymbol{X}} \cdot \left(\overline{\boldsymbol{u}_{\boldsymbol{X}}' \frac{1}{2} |\boldsymbol{u}_{\boldsymbol{X}}'|^2} \right) + \nabla_{\boldsymbol{r}} \cdot \left(\overline{\boldsymbol{\delta u}' \frac{1}{2} |\boldsymbol{u}_{\boldsymbol{X}}'|^2} \right)$$
$$= -\nabla_{\boldsymbol{X}} \cdot (\overline{\boldsymbol{u}_{\boldsymbol{X}}' p'_{\boldsymbol{X}}}) + \frac{\nu}{2} \nabla_{\boldsymbol{X}}{}^2 \frac{1}{2} \overline{|\boldsymbol{u}_{\boldsymbol{X}}'|^2} + \frac{\nu}{2} \nabla_{\boldsymbol{r}}{}^2 \frac{1}{2} \overline{|\boldsymbol{u}_{\boldsymbol{X}}'|^2} - \frac{\nu}{4} \overline{\frac{\partial u_i'^+}{\partial \zeta_k^+} \frac{\partial u_i'^+}{\partial \zeta_k^+}} - \frac{\nu}{4} \overline{\frac{\partial u_i'^-}{\partial \zeta_k^-} \frac{\partial u_i'^-}{\partial \zeta_k^-}}, \tag{2.8}$$

where $P_{\boldsymbol{X}} = -\overline{u'_{\boldsymbol{X}j} u'_{\boldsymbol{X}i}} \frac{\partial \overline{u_{\boldsymbol{X}i}}}{\partial X_j} = -\overline{u'_{\boldsymbol{X}j} u'_{\boldsymbol{X}i}} \frac{1}{2} [\Sigma_{ij}(\boldsymbol{X} + \boldsymbol{r}) + \Sigma_{ij}(\boldsymbol{X} - \boldsymbol{r})]$ and $P^l_{\boldsymbol{X}r} = -\overline{\delta u'_j u'_{\boldsymbol{X}i}}$ $(\partial \delta \overline{u_i} / \partial X_j)$. These two-point turbulence production rates represent linear turbulence fluctuation processes and an exchange of energy between $|\overline{\boldsymbol{u}_{\boldsymbol{X}}}|^2$ and $\overline{|\boldsymbol{u}'_{\boldsymbol{X}}|^2}$ because they appear with opposite signs in (2.7) and (2.8).

Equations (2.3), (2.4) and (2.7), (2.8) offer a powerful and complete set of tools for the analysis of any turbulent flow and can be used to develop two-point turbulence theory

and models which do not have to rely on homogeneity. In particular, (2.4) and (2.8) govern, respectively, the smaller-scale and the larger-scale fluctuating energy contributions to the total turbulent kinetic energy $\frac{1}{2}\overline{|\boldsymbol{u}'^{+}|^2} + \frac{1}{2}\overline{|\boldsymbol{u}'^{-}|^2}$. All physical processes are clearly represented: various turbulent production rates are present as already stated (and the total production rate $P_X + P_r + P^s_{Xr} + P^l_{Xr}$ transfers energy between $\frac{1}{2}|\bar{\boldsymbol{u}}^{+}|^2 + \frac{1}{2}|\bar{\boldsymbol{u}}^{-}|^2$ and $\frac{1}{2}\overline{|\boldsymbol{u}'^{+}|^2} + \frac{1}{2}\overline{|\boldsymbol{u}'^{+}|^2}$); interspace turbulent transport and interscale turbulent transfer rates are represented by conservative terms in $\boldsymbol{X}$ and $\boldsymbol{r}$ spaces, respectively; pressure–velocity terms are also included as are viscous diffusion rates in both $\boldsymbol{X}$ and $\boldsymbol{r}$ spaces and turbulence dissipation rates. In the limit $\boldsymbol{r} \to \boldsymbol{0}$, P_r, P^s_{Xr} and P^l_{Xr} tend to 0 and so do all the terms in (2.3) and (2.4) except the viscous diffusion and dissipation terms which balance by trivial mathematical identity at $\boldsymbol{r} = 0$. However, P_X tends to the one-point turbulence production rate in that limit, and (2.7) and (2.8) tend, respectively, to the one-point mean flow energy and the one-point turbulent kinetic energy equations at $\boldsymbol{X}$. For more details see Hill (2001, 2002), Germano (2007) and Chen & Vassilicos (2022).

3. Interscale turbulent energy transfers

Besides two-point turbulent production terms, the two-point energy equations of the previous section involve important interscale and interspace transport terms. Germano (2007) interpreted his (2.5) and (2.6) in the context of large-eddy simulations. He showed that the term $(\boldsymbol{\delta u}\cdot\boldsymbol{\nabla}_{\boldsymbol{r}})\boldsymbol{u}_{\boldsymbol{X}}$ in (2.5) can be interpreted as the gradient of a subgrid stress. This term gives rise to the term $\boldsymbol{\nabla}_{\boldsymbol{r}}\cdot(\boldsymbol{\delta u}|\boldsymbol{u}_{\boldsymbol{X}}|^2)$ in (2.6) which is therefore an energy transfer rate between large-scale velocities (velocity half-sum) and small-scale velocities (velocity half-difference). Germano (2007) also derived the kinematic equation

$$\boldsymbol{\nabla}_{\boldsymbol{r}}\cdot(\boldsymbol{\delta u}|\boldsymbol{u}_{\boldsymbol{X}}|^2) + \boldsymbol{\nabla}_{\boldsymbol{r}}\cdot(\boldsymbol{\delta u}|\boldsymbol{\delta u}|^2) = 2\boldsymbol{\nabla}_{\boldsymbol{X}}\cdot(\boldsymbol{\delta u}(\boldsymbol{\delta u}\cdot\boldsymbol{u}_{\boldsymbol{X}})) \tag{3.1}$$

which relates $\boldsymbol{\nabla}_{\boldsymbol{r}}\cdot(\boldsymbol{\delta u}|\boldsymbol{u}_{\boldsymbol{X}}|^2)$ to $\boldsymbol{\nabla}_{\boldsymbol{r}}\cdot(\boldsymbol{\delta u}|\boldsymbol{\delta u}|^2)$ in (2.2), where $\boldsymbol{\nabla}_{\boldsymbol{r}}\cdot(\boldsymbol{\delta u}|\boldsymbol{\delta u}|^2)$ accounts for nonlinear interscale energy transfer and the turbulence cascade (see e.g. Chen & Vassilicos 2022).

It must be stressed, however, that the term $\boldsymbol{\nabla}_{\boldsymbol{r}}\cdot(\boldsymbol{\delta u}|\boldsymbol{\delta u}|^2)$ in (2.2) does not only include nonlinear interscale transfer responsible for the turbulence cascade, it also includes two-point turbulence production and interscale energy transfer by mean flow differences. Indeed, it gives rise in (2.4) to the two-point turbulence production rate P_r, to the linear average interscale turbulent energy transfer rate by mean flow differences $\boldsymbol{\delta\bar{u}}\cdot\boldsymbol{\nabla}_{\boldsymbol{r}}\overline{|\boldsymbol{\delta u}'|^2}$ and to the nonlinear average interscale turbulent energy transfer rate $\boldsymbol{\nabla}_{\boldsymbol{r}}\cdot(\overline{\boldsymbol{\delta u}'|\boldsymbol{\delta u}'|^2})$ relating to the turbulence cascade. The other terms in the energy equation (2.4) arise from the pressure gradient, the viscous terms and the advection of small-scale velocity $\boldsymbol{\delta u}$ by the large-scale velocity $\boldsymbol{u}_{\boldsymbol{X}}$ in (2.1). In particular, this advection term gives rise to P^s_{Xr} and to the interspace turbulent transport rate of smaller-scale turbulence energy, i.e. $\boldsymbol{\nabla}_{\boldsymbol{X}}\cdot(\overline{\boldsymbol{u}_{\boldsymbol{X}}'|\boldsymbol{\delta u}'|^2})$.

Similar observations can be made for the large-scale energy equations (2.6) and (2.8) where $\boldsymbol{\nabla}_{\boldsymbol{r}}\cdot(\boldsymbol{\delta u}|\boldsymbol{u}_{\boldsymbol{X}}|^2)$ in (2.6) gives rise in (2.8) to the two-point production rate P^l_{Xr} (not P_X), to the linear average turbulent energy transfer rate by mean flow differences $\boldsymbol{\delta\bar{u}}\cdot\boldsymbol{\nabla}_{\boldsymbol{r}}\overline{|\boldsymbol{u}'_{\boldsymbol{X}}|^2}$ and to the fully nonlinear average turbulent energy transfer rate $\boldsymbol{\nabla}_{\boldsymbol{r}}\cdot(\overline{\boldsymbol{\delta u}'|\boldsymbol{u}'_{\boldsymbol{X}}|^2})$. The other terms in the energy equation (2.8) arise from the pressure gradient, the viscous terms and the self-advection of large-scale velocity $\boldsymbol{u}_{\boldsymbol{X}}$ in (2.5). In particular, this self-advection term gives rise to P_X (not P^l_{Xr}) and to the interspace turbulent transport rate of larger-scale turbulence energy, i.e. $\boldsymbol{\nabla}_{\boldsymbol{X}}\cdot(\overline{\boldsymbol{u}_{\boldsymbol{X}}'|\boldsymbol{u}_{\boldsymbol{X}}'|^2})$.

Returning to the two-point turbulence production terms, P_r and P^s_{Xr} appear in the small-scale energy equation (2.4) whereas P_X and P^l_{Xr} appear in the large-scale energy equation (2.8). All four terms vanish if the mean flow is homogeneous, but P_r represents turbulence production by mean flow non-homogeneities at small scales whereas P_X represents turbulence production by mean flow non-homogeneities at large scales. It is worth noting that P_X tends to the usual one-point turbulence production rate $-\overline{u'_j u'_i}\Sigma_{ij}$ in the limit $\boldsymbol{r} \to \boldsymbol{0}$ ($\boldsymbol{u'}$ is the fluctuating turbulent velocity at one point) whereas P_r tends to zero in that limit. Terms P^l_{Xr} and P^s_{Xr} also tend to zero in that limit but they represent turbulence production by mean flow non-homogeneities that is cross-scale as they involve correlations between the fluctuating velocity half-differences and fluctuating velocity half-sums. The hypothesis that large and small scales may be uncorrelated leads to the suggestion that P^l_{Xr} and P^s_{Xr} may be increasingly negligible for decreasing $|\boldsymbol{r}|$, as indeed found for P^s_{Xr} in the intermediate layer of fully developed turbulent channel flow by Apostolidis, Laval & Vassilicos (2023).

Applying Reynolds averaging to the kinematic identity (3.1) we obtain

$$\begin{aligned}
&\boldsymbol{\nabla}_{\boldsymbol{r}} \cdot (\overline{\boldsymbol{\delta u}|\overline{\boldsymbol{\delta u}}|^2}) + \boldsymbol{\nabla}_{\boldsymbol{r}} \cdot (\overline{\boldsymbol{\delta u}|\boldsymbol{\delta u'}|^2}) + \boldsymbol{\nabla}_{\boldsymbol{r}} \cdot (\overline{\boldsymbol{\delta u'}|\boldsymbol{\delta u'}|^2}) + 2\boldsymbol{\nabla}_{\boldsymbol{r}} \cdot (\overline{\boldsymbol{\delta u'}(\boldsymbol{\delta u'}\overline{\boldsymbol{\delta u}})}) \\
&\quad + \boldsymbol{\nabla}_{\boldsymbol{r}} \cdot (\overline{\boldsymbol{\delta u}|\overline{\boldsymbol{u}_X}|^2}) + \boldsymbol{\nabla}_{\boldsymbol{r}} \cdot (\overline{\boldsymbol{\delta u}|\boldsymbol{u}_{X'}|^2}) + \boldsymbol{\nabla}_{\boldsymbol{r}} \cdot (\overline{\boldsymbol{\delta u'}|\boldsymbol{u}_{X'}|^2}) - 2P^l_{Xr} \\
&= 2\boldsymbol{\nabla}_{\boldsymbol{X}} \cdot (\overline{\boldsymbol{\delta u}(\overline{\boldsymbol{\delta u}} \cdot \overline{\boldsymbol{u}_X})}) + 2\boldsymbol{\nabla}_{\boldsymbol{X}} \cdot (\overline{\overline{\boldsymbol{\delta u}}(\boldsymbol{\delta u'} \cdot \boldsymbol{u'_X})}) \\
&\quad + 2\boldsymbol{\nabla}_{\boldsymbol{X}} \cdot (\overline{\boldsymbol{\delta u'}(\boldsymbol{\delta u'} \cdot \boldsymbol{u'_X})}) + 2\boldsymbol{\nabla}_{\boldsymbol{X}} \cdot (\overline{\boldsymbol{\delta u'}(\overline{\boldsymbol{\delta u}} \cdot \boldsymbol{u'_X})}) - 2P_r,
\end{aligned} \tag{3.2}$$

which demonstrates that, in general, the average interscale turbulent energy transfer rate $\boldsymbol{\nabla}_{\boldsymbol{r}} \cdot (\overline{\boldsymbol{\delta u'}|\boldsymbol{\delta u'}|^2})$ reflecting the turbulence cascade does not trivially relate to the average turbulent energy transfer $\boldsymbol{\nabla}_{\boldsymbol{r}} \cdot (\overline{\boldsymbol{\delta u'}|\boldsymbol{u}_{X'}|^2})$ reflecting work by subgrid stresses (see Germano 2007).

A notable exception is statistically homogeneous turbulence where $\overline{\boldsymbol{\delta u}} = \boldsymbol{0}$, $P_r = 0$, $P^l_{Xr} = 0$ and $\boldsymbol{\nabla}_{\boldsymbol{X}} \cdot (\overline{\boldsymbol{\delta u'}(\boldsymbol{\delta u'} \cdot \boldsymbol{u'_X})}) = 0$ so that (3.2) reduces to

$$\boldsymbol{\nabla}_{\boldsymbol{r}} \cdot \overline{\boldsymbol{\delta u'}|\boldsymbol{u'_X}|^2} = -\boldsymbol{\nabla}_{\boldsymbol{r}} \cdot \overline{\boldsymbol{\delta u'}|\boldsymbol{\delta u'}|^2}. \tag{3.3}$$

If unforced, homogeneous turbulence decays in time. For the past 80 years, grid-generated turbulence has been an attempt to simulate decaying homogeneous turbulence in a wind tunnel (see e.g. Tennekes & Lumley 1972; Pope 2000). In its idealised conception, grid-generated turbulence is such that $\overline{\boldsymbol{u}_X} \cdot \boldsymbol{\nabla}_X \overline{|\boldsymbol{\delta u'}|^2} = \bar{\boldsymbol{u}} \cdot \boldsymbol{\nabla}_X \overline{|\boldsymbol{\delta u'}|^2}$ and $\overline{\boldsymbol{u}_X} \cdot \boldsymbol{\nabla}_X \overline{|\boldsymbol{u'_X}|^2} = \bar{\boldsymbol{u}} \cdot \boldsymbol{\nabla}_X \overline{|\boldsymbol{u'_X}|^2}$ represent turbulence decay following a uniform mean flow ($\overline{\boldsymbol{\delta u}} = \boldsymbol{0}$, $P_r = P_X = P^l_{Xr} = P^s_{Xr} = 0$) and do not vanish, whereas all other terms in (2.4) and (2.8) which are divergences with respect to $\boldsymbol{X}$ do vanish. Under such conditions, and by considering scales $|\boldsymbol{r}|$ large enough to neglect viscous diffusion in $\boldsymbol{r}$ space, fluctuating energy equations (2.4) and (2.8) become, respectively,

$$\overline{\boldsymbol{u}_X} \cdot \boldsymbol{\nabla}_X \overline{|\boldsymbol{\delta u'}|^2} + \boldsymbol{\nabla}_{\boldsymbol{r}} \cdot (\overline{\boldsymbol{\delta u'}|\boldsymbol{\delta u'}|^2}) \approx -\overline{\epsilon'} \tag{3.4}$$

and

$$\overline{\boldsymbol{u}_X} \cdot \boldsymbol{\nabla}_X \overline{|\boldsymbol{u'_X}|^2} + \boldsymbol{\nabla}_{\boldsymbol{r}} \cdot (\overline{\boldsymbol{\delta u'}|\boldsymbol{u'_X}|^2}) \approx -\overline{\epsilon'}, \tag{3.5}$$

where $\overline{\epsilon'}$ is the average turbulence dissipation rate. Kolmogorov's small-scale stationarity hypothesis adapted to these equations states that $\overline{\boldsymbol{u}_X} \cdot \boldsymbol{\nabla}_X \overline{|\boldsymbol{\delta u'}|^2}$ is much smaller in

magnitude than $\overline{\epsilon'}$ at small enough scales $|\boldsymbol{r}|$. With this hypothesis and (3.3) it follows that

$$\boldsymbol{\nabla}_{\boldsymbol{r}} \cdot \overline{\boldsymbol{\delta u'} |\boldsymbol{\delta u'}|^2} \approx -\overline{\epsilon'}, \tag{3.6}$$

$$\boldsymbol{\nabla}_{\boldsymbol{r}} \cdot \overline{\boldsymbol{\delta u'} |\boldsymbol{u'_X}|^2} \approx \overline{\epsilon'} \tag{3.7}$$

and

$$\overline{\boldsymbol{u_X}} \cdot \boldsymbol{\nabla}_{\boldsymbol{X}} \overline{|\boldsymbol{u'_X}|^2} \approx -2\overline{\epsilon'} \tag{3.8}$$

in an intermediate range of scales large enough to neglect viscous diffusion and small enough to neglect small-scale non-stationarity. Relation (3.6) is Kolmogorov's scale-by-scale equilibrium and relation (3.7) was first derived by Germano (2007). (Hosokawa (2007) assumed isotropy and derived the equivalent of (3.7) for homogeneous isotropic turbulence.) Relation (3.8) holds, in fact, for arbitrarily small $\boldsymbol{r}$ and tends to the one-point turbulent kinetic energy equation $\bar{\boldsymbol{u}} \cdot \boldsymbol{\nabla}_{\boldsymbol{X}} \overline{|\boldsymbol{u'}|^2} = -2\overline{\epsilon'}$ in the limit $\boldsymbol{r} \to \boldsymbol{0}$.

Turbulence is rarely homogeneous. Therefore, the natural question to ask is whether energy transfer balances which may be different from but nevertheless in the same spirit as (3.6) and (3.7) exist in non-homogeneous turbulence. And if they do, how different are they and what determines the difference?

Various different classes of non-homogeneity exist. Apostolidis *et al.* (2023) developed a scale-by-scale turbulent kinetic energy balance theory for the intermediate layer of fully developed turbulent channel flow where interspace turbulent transport rate and two-point pressure–velocity transport are negligible but small-scale production is not. A theory of scale-by-scale turbulent kinetic energy for non-homogeneous turbulence was recently proposed by Chen & Vassilicos (2022) whose approach allowed them to treat (2.4) when small-scale interspace turbulent transport and spatial gradients of two-point pressure–velocity correlations are not negligible. In the present paper we study the turbulent flow under rotating blades in a baffled container (mixer) where the baffles break the rotation in the flow and enhance turbulence. We start by assessing two-point production because the theory of Chen & Vassilicos (2022) is designed for flow regions where it makes a negligible or, at the very least, a minor contribution to (2.4). Even in those cases where P_r and P^s_{Xr} are negligible, large-scale two-point production is necessarily present at some scales if one-point production is present in the flow.

In the following section we present our experiment and the PIV used to make the measurements which we use in subsequent sections to estimate various terms in (2.4) and (2.8).

4. Experimental measurements

4.1. *Description of the mixer and experimental configurations*

Experiments are performed with water in the same octagonal shaped, acrylic tank as used in Steiros *et al.* (2017*a*,*b*). The impeller has a radial four-bladed flat-blade turbine, mounted on a stainless steel shaft at the tank's mid-height. The impellers are driven by a stepper motor (Motion Control Products, UK) in microstepping mode (25 000 steps per rotation), to ensure smooth movement, which is controlled by a function generator (33600A, Agilent, USA). The rotation speed and torque signal are measured with a Magtrol torquemeter (TS 106/011). The dimensions of the mixer are presented in figure 2 where $D_T = H = 45$ cm, $C = H/2$ and $D \approx D_T/2$.

Baffles (vertical bars on the sides of the tank) are used to break the rotation of the flow (figure 3). These baffles are designed based on the prescriptions of Nagata (1975) for close

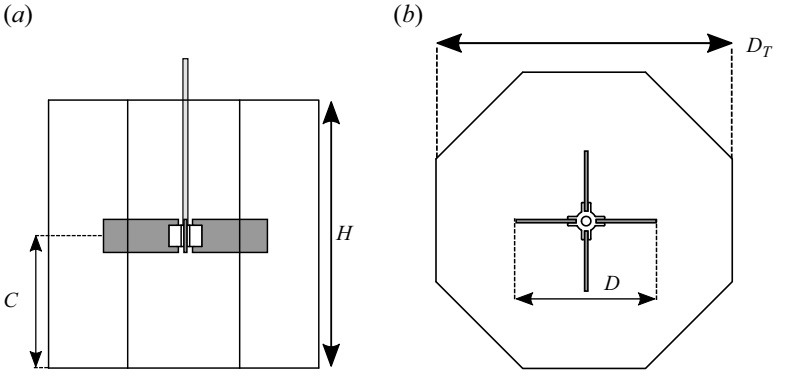

Figure 2. Mixer dimensions. (*a*) Side view. (*b*) Top view. Modified from Steiros *et al.* (2017*b*).

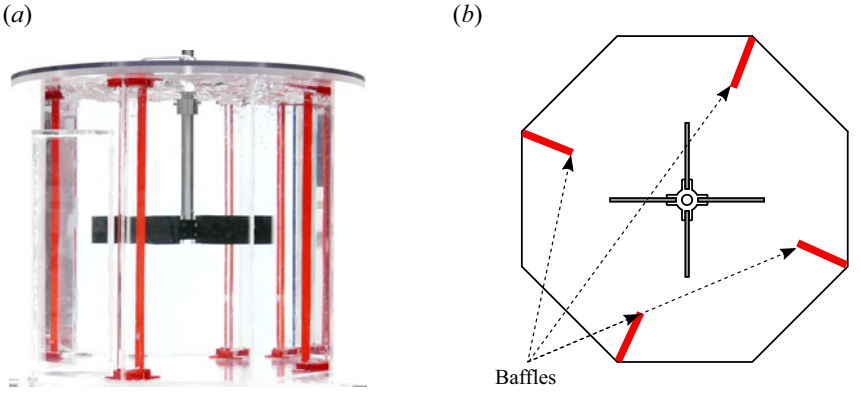

Figure 3. Mixer baffles. (*a*) Mixing tank with baffles. (*b*) Top view of baffles.

to fully baffled conditions which maximise power consumption and minimise rotation. For a circular tank, this condition is achieved with four baffles of width around $0.12D_T$, where D_T is the tank diameter (see D_T in figure 2). Therefore, four baffles of mixer tank height and 58 mm in width are used.

To test the robustness of our results we run experiments with two different types of blade geometry which stimulate the turbulence differently: rectangular blades of 44 mm $\times$ 99 mm size (figure 4*a*) and fractal-like/multiscale blades (figure 4*b*) of the exact same frontal area of 44 $\times$ 99 mm^2 but much longer perimeter. As shown by the PIV measurements of Steiros *et al.* (2017*b*), the two counter-rotating trailing vortices generated by the rotating impeller have the same size roughly equal to the blade half-width for the rectangular blades. Fractal-like blades generate two unequal-sized vortices, but their size is still close to the blade half-width. This blade difference affects turbulence properties substantially as the resulting turbulence dissipation rate differs by 30 % to 40 % at equal rotation speed (see table 3). We use here the two-iteration 'fractal2' blade described in Steiros *et al.* (2017*b*) and shown in figure 4(*b*). Each one of the two types of blade is tested with two different rotor speeds. We therefore conduct experiments in four different configurations. In all cases, the water is filled to the top of the sealed container to minimise the presence of air bubbles in the water.

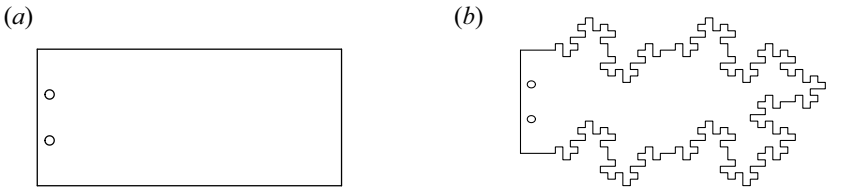

Figure 4. Mixer blades. (*a*) Rectangular blade. (*b*) Fractal-like blade.

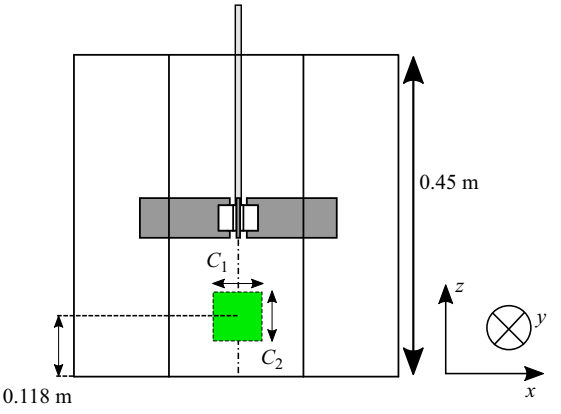

Figure 5. Measurement plane location.

4.2. *Particle image velocimetry settings*

We use 2D2C PIV in the vertical (x, z) plane indicated in figure 5. This figure also shows the field of view which is aligned with that vertical plane and has its centre offset by only 3 ± 1 mm in the y direction from the centreline.

The PIV set-up is composed of a camera, a laser, a set of lenses and mirrors to shape the laser beam into a thin light sheet and a Lavision PTU synchronisation unit and a recording computer with Davis 10 from Lavision.

4.2.1. *Camera*

The camera used is a Phantom v2640 with full sensor image (2048 px $\times$ 1952 px). A Nikon macro Nikkor 200 mm lens is used with f#8. The extremity of the lens is at 93 mm from the glass. The field of view size is $C_1 \times C_2 \approx 27$ mm $\times$ 28 mm (see figure 5) with a magnification factor of 14.1 μm px^{-1}.

The acquisition is done by packets of five time-resolved images. The packet acquisition frequency is 6 Hz to ensure decorrelation between successive packets. The acquisition frequency for the five images within each packet varies from 1.25 to 3 kHz depending on type of blade and rotor speed. This parameter is specifically set for each configuration to ensure a turbulent fluctuation displacement between two frames of around 5 px (corresponding to about 1 standard deviation) and maximum 10 px (observed with samples during the experiments).

4.2.2. *Laser, mirrors and lenses*

The laser used is a Blizz 30W high speed frequency laser from InnoLas. The laser is optimised at 40 kHz with 750 μJ pulse^{-1} at 532 nm wavelength and $M^2 < 1.3$. For the

	F (Hz)	Magnification (μm px^{-1})	Window size (mm)	Window size/η
Rectangular blades	1	14	0.45	4.1
Rectangular blades	1.5	14	0.45	5.1
Fractal blades	1	14	0.45	3.4
Fractal blades	1.5	14	0.45	4.4

Table 1. The PIV resolution.

experiments it was set to around 500 μJ pulse^{-1} because of the smaller frequency used. The laser frequency is set according to the camera time-resolved recording frequency. The focal lengths of the spherical and the cylindrical lenses are $+800$ mm and -80 mm, respectively (beam waist set in the centre of the field of view). The laser sheet height obtained is around 60 mm and its width is 0.6 mm at the waist (which is close to the centreline of the mixer) with a Rayleigh length of 400 mm. Therefore, the laser sheet's width is constant over the field of view.

4.2.3. *Seeding*

Mono-disperse polystyrene Spherotech particles of diameter 5.33 μm are used. They maximise the concentration in the flow and lead to enough particles within each interrogation window. The background noise is around 30 counts. There are on average about 10 particles per interrogation window of 32 px $\times$ 32 px if a threshold of 50 counts is used to select most particles. This is consistent with the criteria of Keane & Adrian (1991). Among these particles, there is on average 6.5 particles higher than 100 counts per interrogation window.

4.2.4. *Processing*

The calibration is done with LaVision 058-5 plate. The PIV processing is done with the Matpiv toolbox modified at LMFL. It is a classical multigrid and multipass cross-correlation algorithm (Willert & Gharib 1991; Soria 1996). Here four passes are used, starting with 64 px $\times$ 64 px, then 48 px $\times$ 48 px and finishing with two 32 px $\times$ 32 px passes. Before the final pass, image deformation is used to improve the results (Scarano 2001; Lecordier & Trinité 2004). An overlap between interrogation windows of 62 % is used, leading to vector spacing of about 0.17 mm. The final grid has then 159 points in the horizontal direction and 167 in the vertical one.

4.3. *Description of the experimental measurements*

4.3.1. *The PIV resolution*

The PIV resolution of the experiment (i.e. interrogation window size) is presented in table 1. In terms of the Kolmogorov length $\eta \equiv (\nu^3/\langle\overline{\epsilon'}\rangle)^{1/4}$, where the angular brackets signify a space average over the PIV field of view, the resolution is between 3.4η and 5.1η depending on configuration. For those configurations where the interrogation window size is higher than 3η the turbulence dissipation rate might be underestimated when denoised properly (Foucaut *et al.* 2021). However, this underestimation remains acceptable for interrogation window size smaller than 5η where less than 30 % of uncertainty (filtering effect) is expected according to Laizet, Nedić & Vassilicos (2015) and Lavoie *et al.* (2007).

4.3.2. *Statistical convergence*

For each configuration, 150 000 velocity fields are recorded in time including 50 000 fully uncorrelated velocity field samples for convergence. Averaging over time is not sufficient for convergence and we therefore also apply averaging over space which greatly improves the convergence. It corresponds to $150\,000 \times 164 \times 78 \approx 1.9 \times 10^9$ points for one-point statistics, where 164×78 is the number of points associated with the vector spacing. For two-point statistics, some spatial points are not available depending on the separation vector size and direction. For zero separation vector, $150\,000 \times 164 \times 78 \approx 1.9 \times 10^9$ points are available for convergence, but for the largest separation vector in the r_x direction there are only $150\,000 \times 164 \approx 2.4 \times 10^7$ points available and in the r_z direction only $150\,000 \times 78 \approx 1.2 \times 10^7$ are available.

The most important results in this paper are reported with error bars quantifying convergence and computed with a bootstrapping method. The central limit theorem is applied to averages over subgroups of samples of the quantity of interest. For each quantity, 600 subgroups containing 83 time steps with at least 159 spatial points are used for the computation of an error bar. This method is robust and provides accurate estimations without having to define the number of independent points. The resulting error bars are also representative of the convergence of third-order two-point statistics plotted here without error bars as the number of points used is the same.

4.3.3. *Peak locking*

When a particle is too small, its correlation peak position fitting results are biased towards integer values. Therefore, the displacement between two images is more likely to be an integer number of pixels. This peak-locking error (as it is called; Raffel *et al.* 2018) is systematic (bias error) and is therefore visible on the velocity probability distribution functions (sine modulation) but does not usually impact mean quantities of turbulent flow if enough dynamic is used (here high dynamic is selected of about 5 px for one standard deviation; see Christensen (2004)). Peak locking can be reduced by increasing particle diffraction spot using camera lens aperture f# number. However, an increased f# number reduces the brightness of the particles and therefore the number of visible particles. In this experiment, f#8 is used as a compromise and some peak locking is still visible. The impact on the results is analysed in § 3 of the supplementary material available at https://doi.org/10.1017/jfm.2024.220 where we show that energy spectra and averages of two-point velocity quantities such as the interscale turbulent energy transfer rate are unaffected by peak locking.

4.3.4. *Defining parameters*

The defining parameters of the experiment are presented in table 2. The rotation frequency F is either 1 or 1.5 Hz. The global Reynolds number is $Re = 2\pi FR^2/\nu$, where $R = D/2 \approx 11.25$ cm is an estimate of the rotor radius. The value of Re is large, higher than 8×10^4, and the flow is therefore turbulent.

The Rossby number is estimated as $Ro = U/2\Omega R$, where U (following Baroud *et al.* 2002) is the maximum fluctuating velocity in all our samples, R is as an estimate of the integral length scale of the turbulence and $\Omega = 2\pi F$. Our values of Ro range between 10^{-1} and 1 and are therefore intermediate between those of fast-rotating and non-rotating turbulence. However, the rotor rotation speed Ω is not representative of flow rotation because the baffles break the flow rotation as explained in Nagata (1975). Therefore, the

	F (Hz)	Re	vel r.m.s. (m s^{-1})	Ro	Mean torque (N m)
Rectangular blades	1	9.8×10^4	1.0×10^{-1}	3.6×10^{-1}	5.3×10^{-1}
Rectangular blades	1.5	1.3×10^5	1.6×10^{-1}	4.0×10^{-1}	1.1
Fractal blades	1	8.6×10^4	9.1×10^{-2}	3.2×10^{-1}	4.1×10^{-1}
Fractal blades	1.5	1.2×10^5	1.4×10^{-1}	3.4×10^{-1}	8.1×10^{-1}

Table 2. Main parameters of the experiment: vel r.m.s. (m s^{-1}) stands for $\sqrt{\overline{\langle u_x'^2 \rangle} + \overline{\langle u_z'^2 \rangle}}$.

	F (Hz)	$\langle \overline{\epsilon'} \rangle$ (m^2 s^{-3})	η (m)	λ (m)	Re_λ
Rectangular blades	1	3.6×10^{-3}	1.1×10^{-4}	4.1×10^{-3}	5.1×10^2
Rectangular blades	1.5	1.2×10^{-2}	8.8×10^{-5}	3.7×10^{-3}	6.5×10^2
Fractal blades	1	2.4×10^{-3}	1.3×10^{-4}	4.9×10^{-3}	4.8×10^2
Fractal blades	1.5	8.2×10^{-3}	1.0×10^{-4}	4.1×10^{-3}	5.8×10^2

Table 3. Main turbulence parameters. The Kolmogorov length scale is calculated as $\eta \equiv (\nu^3/\langle \overline{\epsilon'} \rangle)^{1/4}$. The Taylor length and the Reynolds number Re_λ are calculated as in § 1.2 of the supplementary material.

Rossby number is probably severely underestimated and the rotation is not expected to affect significantly the turbulence behaviour in our experiment.

4.3.5. *Basic turbulent flow properties*

The main turbulent parameters are presented in table 3. They include the turbulence dissipation rate $\langle \overline{\epsilon'} \rangle$ averaged over time (overbar) and over space in our field of view (angle brackets), the resulting Kolmogorov length scale η (computed with $\langle \overline{\epsilon'} \rangle$) and the Taylor length λ. These parameters are provided as reference and are used in the paper to non-dimensionalise results.

The Taylor-length-based Reynolds number Re_λ (see discussion on its estimation in § 1.2 of the supplementary material) is higher than 480 in all four configurations. All the four flows that we study are therefore highly turbulent.

In figure 6(*b*) we plot the mean flow velocity for one of our four configurations but the plot is representative of all four configurations. The mean flow velocity is oriented vertically from bottom to top and is not negligible in magnitude. Within our field of view, it is horizontally uniform and accelerates by about 7 % from bottom to top. These observations are consistent with the overall mean flow structure identified by Nagata (1975) and shown in figure 6(*a*).

4.3.6. *Two-dimensional two-component truncations and estimates of three-dimensional three-component statistics*

The various terms in the equations of the previous sections require three-component velocity fields in three-dimensional space to be calculated. However, our measurements are performed with 2D2C PIV. We can therefore only calculate 2D2C truncations of three-dimensional three-component (3D3C) statistics and in a few cases (§§ 5 and 6) we estimate 2D2C surrogates of 3D3C terms.

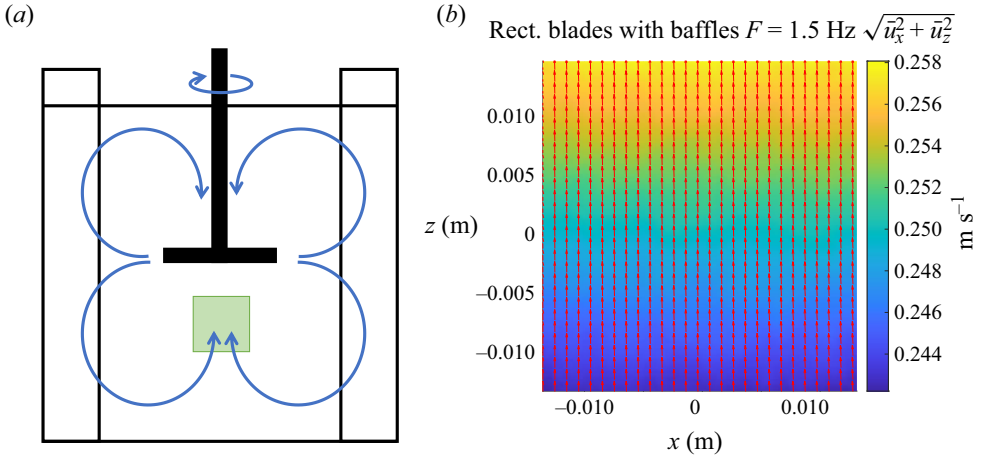

Figure 6. (*a*) Schematic of mean flow in a mixer with baffles (Nagata 1975). (*b*) Mean flow measurement within the measurement plane shown as a green square in (*a*).

5. Two-point turbulence production rates

We start our data analysis with an assessment of two-point turbulence production rates. We define our coordinate system such that components $i = 1$, $i = 2$ and $i = 3$ correspond to the x, y and z directions, respectively, and therefore $(r_1, r_2, r_3) = (r_x, r_y, r_z)$ and $(X_1, X_2, X_3) = (X_x, X_y, X_z)$. The sums defining $P_r = -\overline{\delta u_j' \delta u_i'}(\partial \delta \overline{u_i}/\partial r_j)$, $P^s_{Xr} = -\overline{u'_{Xj} \delta u_i'}(\partial \delta \overline{u_i}/\partial X_j)$, $P_X = -\overline{u'_{Xj} u'_{Xi}}(\partial \overline{u_{Xi}}/\partial X_j)$ and $P^l_{Xr} = -\overline{\delta u_j' u'_{Xi}}(\partial \delta \overline{u_i}/\partial X_j)$ are sums of nine terms of which our 2D2C PIV has access to four. Our data therefore allow only truncations to be calculated directly and we start with the truncation of P_r:

$$\widetilde{P}_r = -\overline{\delta u_x' \delta u_x'} \frac{\partial \overline{\delta u_x}}{\partial r_x} - \overline{\delta u_x' \delta u_z'} \frac{\partial \overline{\delta u_z}}{\partial r_x} - \overline{\delta u_z' \delta u_x'} \frac{\partial \overline{\delta u_x}}{\partial r_z} - \overline{\delta u_z' \delta u_z'} \frac{\partial \overline{\delta u_z}}{\partial r_z} \tag{5.1}$$

with

$$\overline{\delta u_y' \delta u_y'} \frac{\partial \overline{\delta u_y}}{\partial r_y} + \overline{\delta u_x' \delta u_y'} \frac{\partial \overline{\delta u_y}}{\partial r_x} + \overline{\delta u_x' \delta u_y'} \frac{\partial \overline{\delta u_x}}{\partial r_y} + \overline{\delta u_z' \delta u_y'} \frac{\partial \overline{\delta u_y}}{\partial r_z} + \overline{\delta u_z' \delta u_y'} \frac{\partial \overline{\delta u_z}}{\partial r_y} \tag{5.2}$$

being the difference between $\widetilde{P}_r$ and P_r. We know from our measurements and from Nagata (1975) that the mean flow is vertical in our field of view which is small and very close to the centreline of the tank. Hence, we can readily neglect all the terms making the difference between $\widetilde{P}_r$ and P_r except $\overline{\delta u_z' \delta u_y'}(\partial \overline{\delta u_z}/\partial r_y)$. Making the assumption that $\overline{\delta u_z' \delta u_y'}(\partial \overline{\delta u_z}/\partial r_y) \approx \overline{\delta u_z' \delta u_x'}(\partial \overline{\delta u_z}/\partial r_x)$ we form the following surrogate estimate of P_r:

$$\widetilde{\widetilde{P}}_r = -\overline{\delta u_x' \delta u_x'} \frac{\partial \overline{\delta u_x}}{\partial r_x} - 2\overline{\delta u_x' \delta u_z'} \frac{\partial \overline{\delta u_z}}{\partial r_x} - \overline{\delta u_z' \delta u_x'} \frac{\partial \overline{\delta u_x}}{\partial r_z} - \overline{\delta u_z' \delta u_z'} \frac{\partial \overline{\delta u_z}}{\partial r_z}. \tag{5.3}$$

Similarly, we have the following truncations and surrogate estimates for the other three two-point turbulence production rates:

$$\widetilde{P^s_{Xr}} = -\overline{u'_{Xx} \delta u_x'} \frac{\partial \overline{\delta u_x}}{\partial X_x} - \overline{u'_{Xx} \delta u_z'} \frac{\partial \overline{\delta u_z}}{\partial X_x} - \overline{u'_{Xz} \delta u_x'} \frac{\partial \overline{\delta u_x}}{\partial X_z} - \overline{u'_{Xz} \delta u_z'} \frac{\partial \overline{\delta u_z}}{\partial X_z} \tag{5.4}$$

and

$$\widetilde{\widetilde{P^s_{Xr}}} = -\overline{u'_{Xx}\delta u'_x}\frac{\partial\overline{\delta u_x}}{\partial X_x} - 2\overline{u'_{Xx}\delta u'_z}\frac{\partial\overline{\delta u_z}}{\partial X_x} - \overline{u'_{Xz}\delta u'_x}\frac{\partial\overline{\delta u_x}}{\partial X_z} - \overline{u'_{Xz}\delta u'_z}\frac{\partial\overline{\delta u_z}}{\partial X_z}; \tag{5.5}$$

$$\widetilde{P_X} = -\overline{u'_{Xx}u'_{Xx}}\frac{\partial\overline{u_{Xx}}}{\partial X_x} - \overline{u'_{Xx}u'_{Xz}}\frac{\partial\overline{u_{Xz}}}{\partial X_x} - \overline{u'_{Xz}u'_{Xx}}\frac{\partial\overline{u_{Xx}}}{\partial X_z} - \overline{u'_{Xz}u'_{Xz}}\frac{\partial\overline{u_{Xz}}}{\partial X_z} \tag{5.6}$$

and

$$\widetilde{\widetilde{P_X}} = -\overline{u'_{Xx}u'_{Xx}}\frac{\partial\overline{u_{Xx}}}{\partial X_x} - 2\overline{u'_{Xx}u'_{Xz}}\frac{\partial\overline{u_{Xz}}}{\partial X_x} - \overline{u'_{Xz}u'_{Xx}}\frac{\partial\overline{u_{Xx}}}{\partial X_z} - \overline{u'_{Xz}u'_{Xz}}\frac{\partial\overline{u_{Xz}}}{\partial X_z}; \tag{5.7}$$

$$\widetilde{P^l_{Xr}} = -\overline{\delta u'_x u'_{Xx}}\frac{\partial\overline{\delta u_x}}{\partial X_x} - \overline{\delta u'_x u'_{Xz}}\frac{\partial\overline{\delta u_z}}{\partial X_x} - \overline{\delta u'_z u'_{Xx}}\frac{\partial\overline{\delta u_x}}{\partial X_z} - \overline{\delta u'_z u'_{Xz}}\frac{\partial\overline{\delta u_z}}{\partial X_z} \tag{5.8}$$

and

$$\widetilde{\widetilde{P^l_{Xr}}} = -\overline{\delta u'_x u'_{Xx}}\frac{\partial\overline{\delta u_x}}{\partial X_x} - 2\overline{\delta u'_x u'_{Xz}}\frac{\partial\overline{\delta u_z}}{\partial X_x} - \overline{\delta u'_z u'_{Xx}}\frac{\partial\overline{\delta u_x}}{\partial X_z} - \overline{\delta u'_z u'_{Xz}}\frac{\partial\overline{\delta u_z}}{\partial X_z}. \tag{5.9}$$

The results are presented in § 2 of the supplementary material and our data support the hypothesis already expressed at the end of the fourth paragraph of § 3 that, for the turbulent flows considered here and for scales small enough compared to the large scales of the flow, two-point production P^s_{Xr} may be neglected in the small-scale energy equation (2.4). However, P_r, while smaller than all other terms, may not be convincingly negligible in that equation. In the intermediate layer of fully developed turbulent channel flow, P_r was also found by Apostolidis *et al.* (2023) not to be negligible at scales comparable to and larger than the Taylor length, but the ratio of P_r to turbulence dissipation rate was significantly higher than in the present flow. The supplementary material also includes results for P_X and P^l_{Xr} in its § 2, suggesting that P^l_{Xr} may but P_X may not be negligible in the large-scale energy equation (2.8).

6. Small-scale linear transport terms

In the theory used in the present paper, we neglect two-point production in the small-scale energy equation (2.4) but not in the large-scale energy equation (2.8). We return to this approximation at the start of § 8.4. We now focus on (2.4) and ask whether we can justify simplifying it further by neglecting the linear transport rate $(\overline{\boldsymbol{u_X}}\cdot\boldsymbol{\nabla_X}+\boldsymbol{\delta\bar{u}}\cdot\boldsymbol{\nabla_r})\frac{1}{2}\overline{|\boldsymbol{\delta u'}|^2}$. The results are presented in § 2 of the supplementary material where we find grounds to neglect some but not all of the terms in $(\overline{\boldsymbol{u_X}}\cdot\boldsymbol{\nabla_X}+\boldsymbol{\delta\bar{u}}\cdot\boldsymbol{\nabla_r})\frac{1}{2}\overline{|\boldsymbol{\delta u'}|^2}$ from the small-scale energy equation (2.4) at small enough scales. Note, however, that the conclusions of the following two sections can be obtained (see Chen & Vassilicos 2022) both with and without this term in (2.4) (with the only potential exception of the last sentence of § 8.4 which may need to be qualified). For ease of presentation we therefore consider the following simplified form of this equation for the turbulent flow region studied here:

$$\begin{aligned}&\boldsymbol{\nabla_X}\cdot(\overline{\boldsymbol{u_{X'}}|\boldsymbol{\delta u'}|^2})+\boldsymbol{\nabla_r}\cdot(\overline{\boldsymbol{\delta u'}|\boldsymbol{\delta u'}|^2})+2\boldsymbol{\nabla_X}\cdot\overline{(\boldsymbol{\delta u'}\delta p')}\\ &\quad\approx\frac{\nu}{2}(\boldsymbol{\nabla_X}^2+\boldsymbol{\nabla_r}^2)\overline{|\boldsymbol{\delta u'}|^2}-\frac{1}{2}\left(\overline{\epsilon'^+}+\overline{\epsilon'^-}\right),\end{aligned} \tag{6.1}$$

where $\overline{\epsilon'^+}$ and $\overline{\epsilon'^-}$ are $\overline{\epsilon'}$ at $\boldsymbol{\zeta}^+$ and $\boldsymbol{\zeta}^-$, respectively.

It is worth pointing out that a careful look at the results in § 2 of the supplementary material suggests that the approximation (6.1) does not necessarily hold for large enough values of r_x and/or r_z. Apostolidis *et al.* (2023) found, in a very different non-homogeneous turbulent flow (namely the intermediate region of fully developed turbulent channel flow), that (6.1) is not a representative approximation at scales comparable with and larger than λ whereas we do assume it to be a good approximation at such scales (if they are not too large) in the flow region of the non-homogeneous turbulent flows considered here.

7. Second-order structure functions

We now adopt the approach of Chen & Vassilicos (2022) which is based on inner and outer similarity. In effect, we assume that regions of space exist in the flow where the nonlinear and non-local dynamics of the small-scale turbulence are similar at different places within the region. We therefore start with a hypothesis of inner and outer similarity for the second-order structure function $\overline{|\boldsymbol{\delta u'}|^2}$, namely

$$\overline{|\boldsymbol{\delta u'}|^2} = V_{O2}^2(\boldsymbol{X}) f_{O2}\left(\frac{\boldsymbol{r}}{l_O}\right) \tag{7.1}$$

for $|\boldsymbol{r}| \gg l_I$ and

$$\overline{|\boldsymbol{\delta u'}|^2} = V_{I2}^2(\boldsymbol{X}) f_{I2}\left(\frac{\boldsymbol{r}}{l_I}\right) \tag{7.2}$$

for $|\boldsymbol{r}| \ll l_O$, where the inner length scale l_I depends on viscosity and is much smaller than the outer length scale l_O which does not depend on viscosity, i.e. $l_I = l_I(\boldsymbol{X}) \ll l_O = l_O(\boldsymbol{X})$ for large enough Reynolds number. The outer length scale can be thought of as an integral length of the order of the blade size $R = D/2$ and is assumed to be smaller than the extent of the similarity region where (7.1) and (7.2) hold. Statistical homogeneity is a special case of our inner and outer similarity hypotheses where V_{O2}, V_{I2}, l_O and l_I are independent of $\boldsymbol{X}$. In the following section we apply the approach of Chen & Vassilicos (2022) to the small-scale energy balance (6.1).

It is natural to expect the outer characteristic velocity V_{O2} to be independent of viscosity but the inner characteristic velocity V_{I2} to depend on it. The ratios V_{I2}/V_{O2} and l_I/l_O must therefore be functions of a local Reynolds number $Re_O = V_{O2}l_O/\nu$ and we write $V_{I2}/V_{O2} = g_2(Re_O, \boldsymbol{X})$, $l_I/l_O = g_l(Re_O, \boldsymbol{X})$, these two functions having to tend to zero as Re_O tends to infinity. This is the only assumption we make about these two ratios V_{I2}/V_{O2} and l_I/l_O. In § 8.2 we obtain their Re_O dependence from the small-scale turbulent energy budget, i.e. from the Navier–Stokes equation.

The inner and outer similarity forms overlap in the range $l_I \ll |\boldsymbol{r}| \ll l_O$, hence

$$f_{O2}\left(\frac{\boldsymbol{r}}{l_O}\right) = g_2^2(Re_O, \boldsymbol{X}) f_{I2}\left(\frac{\boldsymbol{r}}{l_O} g_l^{-1}\right) \tag{7.3}$$

in this intermediate range. Given that the left-hand side of this equation does not depend on Re_O, the derivative with respect to Re_O of the right-hand side cancels and we obtain

$$g_l \frac{\mathrm{d}g_2^2}{\mathrm{d}Re_O} f_{I2}(\boldsymbol{\rho}) = g_2^2 \frac{\mathrm{d}g_l}{\mathrm{d}Re_O} \rho_j \frac{\partial}{\partial \rho_j} f_{I2}(\boldsymbol{\rho}), \tag{7.4}$$

where there is an implicit sum over $j = 1, 2, 3$ and $\boldsymbol{\rho} = (\rho_1, \rho_2, \rho_3) = \boldsymbol{r}/l_I$. It follows that $\rho_j(\partial/\partial\rho_j) f_{I2}(\boldsymbol{\rho})$ is proportional to $f_{I2}(\boldsymbol{\rho})$. To solve for f_{I2} we adopt spherical coordinates

(ρ, θ, ϕ) for $\boldsymbol{\rho}$, where θ varies from 0 to π and vanishes if $\boldsymbol{\rho}$ is aligned with the y axis and where ϕ varies from 0 to 2π and is equal to 0 or $\pi/2$ if $\boldsymbol{\rho}$ is aligned with the x or the z axis, respectively. The proportionality between $\rho_j(\partial/\partial\rho_j)f_{I2}(\boldsymbol{\rho})$ and $f_{I2}(\boldsymbol{\rho})$ becomes $nf_{I2}(\rho, \theta, \phi) = \rho(\partial/\partial\rho)f_{I2}(\rho, \theta, \phi)$ in terms of a dimensionless proportionality constant n and the solution to this equation is

$$f_{I2} = \rho^n F(\theta, \phi), \tag{7.5}$$

where F is an unknown function of angles θ and ϕ. Note that (7.5) holds in the intermediate range $l_I \ll |\boldsymbol{r}| \ll l_O$. Returning to (7.3), we get

$$g_2^2(Re_O, \boldsymbol{X})g_l^{-n}(Re_O, \boldsymbol{X}) = A_1, \tag{7.6}$$

where the dimensionless coefficient A_1 is independent of Re_O and $\boldsymbol{X}$.

At this stage we follow Chen & Vassilicos (2022) and use their hypothesis of inner–outer equivalence for dissipation according to which there is an inner and an outer way to estimate the turbulence dissipation rate: $\overline{\epsilon'} \sim V_{O2}^3/l_O \sim V_{I2}^3/l_I$, where the proportionality coefficients are independent of Re_O but can depend on $\boldsymbol{X}$. We actually derive this hypothesis in § 8.3 and our derivation shows clearly that it has nothing to do with Kolmogorov's scale-by-scale equilibrium. At this stage, it provides the additional constraint $g_2^3(Re_O)g_l^{-1}(Re_O) = A_2$, where the coefficient A_2 is independent of Re_O. Combined with this additional constraint, (7.6) yields $n = 2/3$ (and $A_3 = A^{3/2}$, which means that A_2 is also independent of $\boldsymbol{X}$) and therefore

$$\overline{|\boldsymbol{\delta u'}|^2} = C(\overline{\epsilon'}r)^{2/3}F(\theta, \phi) \tag{7.7}$$

in the intermediate range $l_I \ll r = |\boldsymbol{r}| \ll l_O$. Note that, reflecting the dimensionless coefficients in $\overline{\epsilon'} \sim V_{O2}^3/l_O \sim V_{I2}^3/l_I$, the dimensional coefficient C can vary in space but is independent of Reynolds number. The dependence of these dimensional coefficients, and C in particular, on spatial position is an obvious difference from Kolmogorov's prediction for the second-order structure function which is limited to locally homogeneous turbulence. This difference highlights the underlying difference in the way that our result (7.7) was obtained compared with Kolmogorov's derivation of his corresponding prediction which resembles (7.7) in the scaling $(\overline{\epsilon'}r)^{2/3}$ but is otherwise different (see Frisch (1995), Pope (2000) and § 2 of Chen & Vassilicos (2022)).

We can refine our hypothesis of similarity by replacing it with a hypothesis of isotropic similarity which is a hypothesis of similarity for each component of $\boldsymbol{\delta u'}$, namely

$$\overline{(\delta u_j')^2} = V_{O2}^2(\boldsymbol{X})f_{O2,j}\left(\frac{\boldsymbol{r}}{l_O}\right) \tag{7.8}$$

for $|\boldsymbol{r}| \gg l_I$ and

$$\overline{(\delta u_j')^2} = V_{I2}^2(\boldsymbol{X})f_{I2,j}\left(\frac{\boldsymbol{r}}{l_I}\right) \tag{7.9}$$

for $|\boldsymbol{r}| \ll l_O$ for every $j = 1, 2, 3$. This is not an assumption of isotropy because neither the functions $f_{O2,j}$ nor the functions $f_{I2,j}$ are necessarily the same for different $j = 1, 2, 3$. The argument leading to (7.7) can be repeated for every $j = 1, 2, 3$ yielding

$$\overline{(\delta u_j')^2} = C_j(\overline{\epsilon'}r)^{2/3}F_j(\theta, \phi) \tag{7.10}$$

in the intermediate range $l_I \ll r = |\boldsymbol{r}| \ll l_O$. The dimensionless coefficient C_j may vary with j and with $\boldsymbol{X}$ and the dimensionless function F_j, which is independent of $\boldsymbol{X}$ and

of $r \equiv |\boldsymbol{r}|$, may also vary with j. The determination of the inner length scale l_I requires the small-scale energy balance (6.1). This is done in § 8. We complete the present section by confronting prediction (7.10) with our PIV data. This prediction is similar to Kolmogorov's prediction for second-order structure functions but it was derived without the homogeneity assumption required by Kolmogorov's theory and without Kolmogorov's scale-by-scale equilibrium which forms the physical basis of Kolmogorov's dimensional analysis.

7.1. *Second-order structure function measurements*

We compute the normalised structure functions $\langle \overline{(\delta u_j')^2}/\overline{\epsilon'}^{2/3} \rangle$ for $j = 1$ (velocity fluctuations along the x axis) and $j = 3$ (velocity fluctuations along the z axis) by averaging over time, i.e. over our 150 000 samples (which correspond to 50 000 uncorrelated samples), and also averaging over $\boldsymbol{X}$, i.e. over the planar space of our field of view. The additional averaging over space is necessary for convergence of our statistics (see in § 4 in the supplementary material). The normalised structure functions $\overline{(\delta u_j')^2}/\overline{\epsilon'}^{2/3}$ are therefore calculated by averaging over available points in the field of view in 150 000 velocity field samples in this field of view. For two-point statistics, there are between 1.2×10^7 and 1.9×10^9 points available for convergence, depending on two-point separation vector, using both space and time averaging as explained in § 4.3.2.

Given that (7.10) implies $\langle \overline{(\delta u_j')^2}/\overline{\epsilon'}^{2/3} \rangle = \langle C_j \rangle r^{2/3} F_j(\theta, \phi)$, we plot in figure 7 the compensated structure functions $\langle \overline{(\delta u_x')^2}/\overline{\epsilon'}^{2/3} \rangle r^{-2/3}$ ($j = 1$) versus r_x/D (figure 7*a*) and versus r_z/D (figure 7*b*) and $\langle \overline{(\delta u_z')^2}/\overline{\epsilon'}^{2/3} \rangle r^{-2/3}$ ($j = 3$) versus r_x/D (figure 7*c*) and versus r_z/D (figure 7*d*). This is the intermediate-range data collapse suggested by (7.10) for all four configurations considered here. The dependence on r_x represents the dependence on r for $\theta = \pi/2$ and $\phi = 0$ whereas the dependence on r_z represents the dependence on r for $\theta = \pi/2$ and $\phi = \pi/2$. The average turbulence dissipation rate $\langle \overline{\epsilon'} \rangle$ varying by a factor larger than 4 across our four different configurations (see table 3), figure 7 suggests that the collapse of the compensated structure functions in figure 7 is satisfactory. The exponent of the power-law dependence of these structure functions on r_x and r_z (in an expected intermediate range of scales much smaller than $R = D/2$) appears close to but not exactly $2/3$ and seems to vary a little around $2/3$ from plot to plot in figure 7. The theory presented above and yielding (7.7) and (7.10) may be a leading-order theory with different higher-order corrections for different j components. Such corrections are beyond the scope of the present paper, but noting from the plots in figure 7 that there may be opposite corrections to the $2/3$ scaling, we now consider the r_x and r_z dependencies of the normalised structure function $\langle \overline{(\delta u_x'^2 + \delta u_z'^2)}/\overline{\epsilon'}^{2/3} \rangle$. Equation (7.10) implies

$$\langle \overline{(\delta u_x'^2 + \delta u_z'^2)}/\overline{\epsilon'}^{2/3} \rangle = r^{2/3}[\langle C_1 \rangle F_1(\theta, \phi) + \langle C_3 \rangle F_3(\theta, \phi)]. \tag{7.11}$$

This compensated normalised structure function is presented in figure 8 as a function of r_x/D (i.e. r/D for $\theta = \pi/2$ and $\phi = 0$) in one plot and of r_z/D (i.e. r/D for $\theta = \pi/2$ and $\phi = \pi/2$) in the other. Once again, the resulting collapse of the structure functions for the four different configurations is acceptable given the wide variation of $\langle \overline{\epsilon'} \rangle$ from one configuration to the other. To look at the power-law scaling more finely, we estimate the logarithmic slopes of $S \equiv \langle \overline{(\delta u_x'^2 + \delta u_z'^2)}/\overline{\epsilon'}^{2/3} \rangle$ versus both r_x and r_z, i.e. $\mathrm{d}\log S/\mathrm{d}\log r_x$ and $\mathrm{d}\log S/\mathrm{d}\log r_z$, which we plot versus r_x and r_z, respectively, in figures 9(*a*) and 9(*b*).

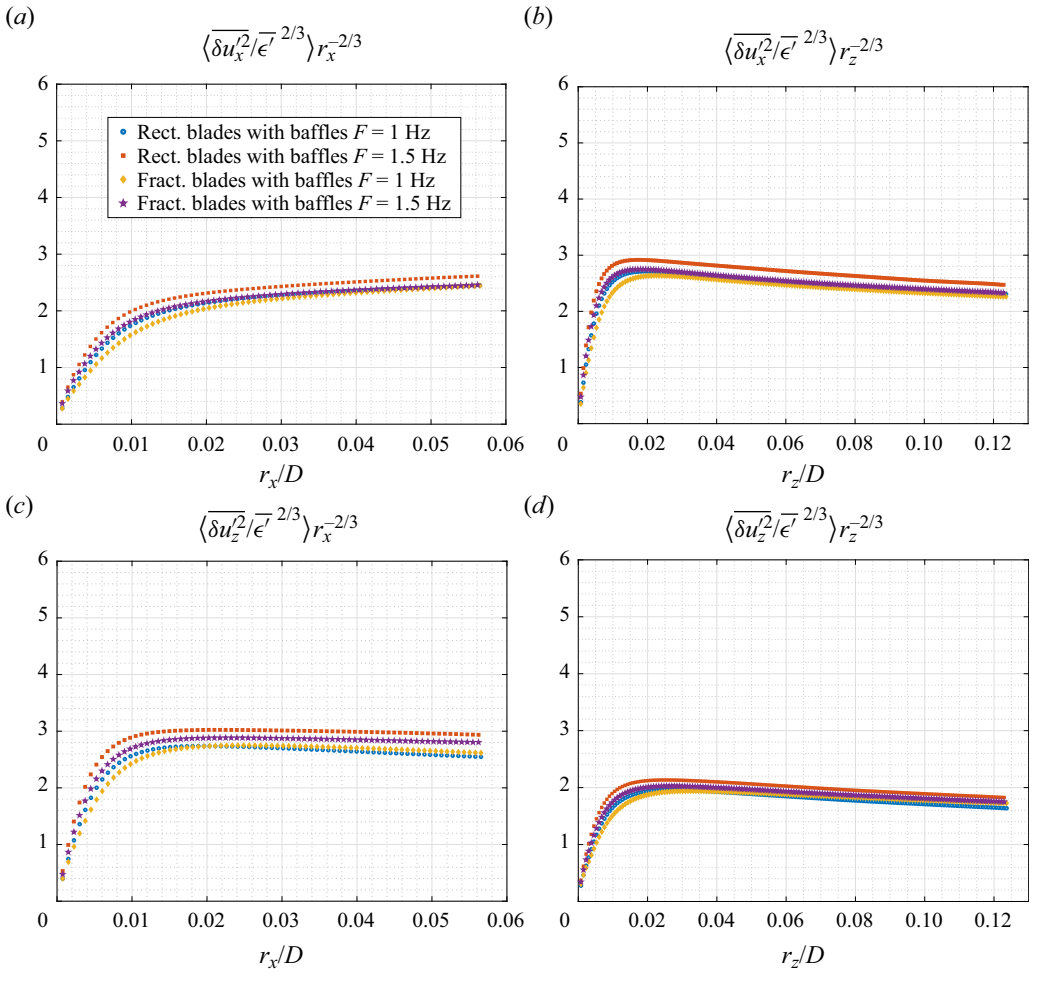

Figure 7. Compensated structure functions. (*a*) Compensated $\overline{\delta u_x'^2}$ in r_x direction. (*b*) Compensated $\overline{\delta u_x'^2}$ in r_z direction. (*c*) Compensated $\overline{\delta u_z'^2}$ in r_x direction. (*d*) Compensated $\overline{\delta u_z'^2}$ in r_z direction.

A well-defined plateau appears in both directions for $r_x, r_z \ll R = D/2$ which confirms the power-law behaviour of S. The value of the plateau is the power-law exponent and it is slightly different in the two directions: it lies between $2/3 \approx 0.66$ and 0.7 in the r_x direction, which is very close to the theory's prediction, but between 0.5 and 0.6 in the r_z direction, which is further away from it.

We must leave it for future study to determine whether the deviation from $n = 2/3$ that we observe in the vertical r_z direction is a finite-Reynolds-number effect or whether it results from deviations from outer and/or inner isotropic similarity of second-order structure functions. The good agreement with $n = 2/3$ in the r_x direction is nevertheless encouraging and so, in the following section, we use $n = 2/3$ in conjunction with an analysis of the small-scale energy budget to predict the relations between l_I and l_O and between V_{I2} and V_{O2}. Perhaps more importantly, though, this analysis also leads to predictions concerning nonlinear interscale and interspace turbulent energy transfer rates which do not critically depend on the value of the exponent n and which we also subject to experimental checks.

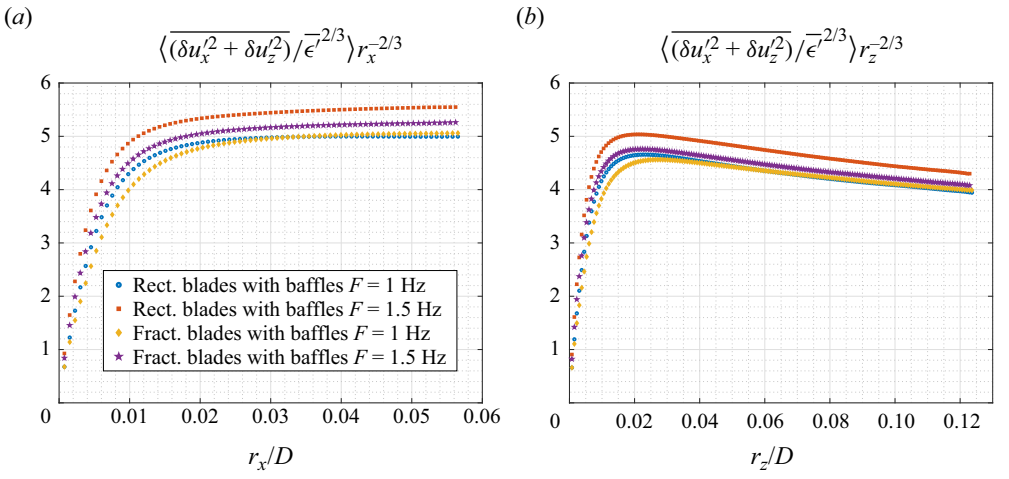

Figure 8. Compensated structure function $\overline{(\delta u_x'^2 + \delta u_z'^2)}$. (*a*) The r_x direction. (*b*) The r_z direction.

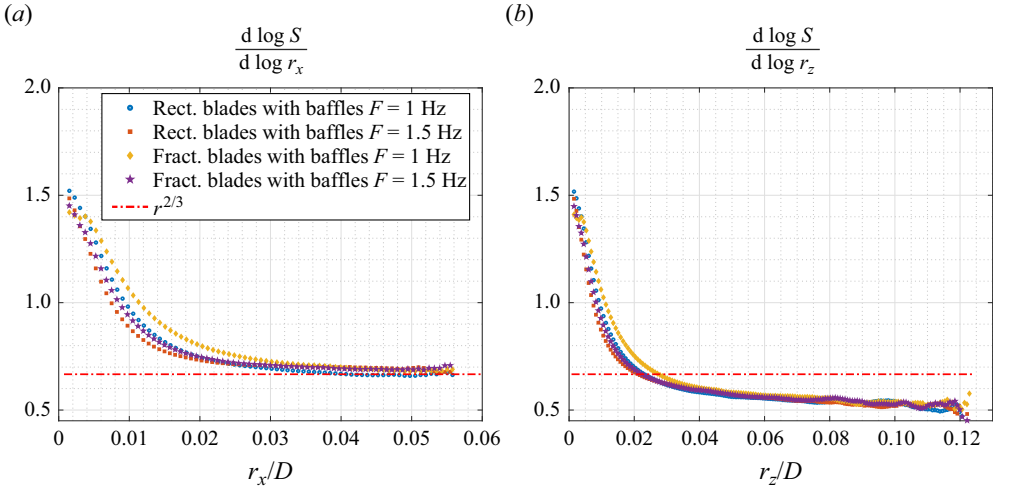

Figure 9. Logarithmic slope of $S \equiv \langle\overline{(\delta u_x'^2 + \delta u_z'^2)}/\overline{\epsilon'}^{2/3}\rangle$. (*a*) The r_x direction. (*b*) The r_z direction.

8. Small-scale turbulent energy budgets

Following Chen & Vassilicos (2022) who assume that regions exist in the flow where the nonlinear and non-local dynamics of the small scale turbulence are similar at different places within the region, we now introduce, for such a region, inner and outer similarity form for every term on the left-hand side of (6.1).

Outer similarity for $|\boldsymbol{r}| \gg l_I$:

$$\boldsymbol{\nabla}_X \cdot (\overline{\boldsymbol{u}_{X'}|\boldsymbol{\delta u}'|^2}) = \frac{V_{OX}^3(\boldsymbol{X})}{l_O} f_{OX}\left(\frac{\boldsymbol{r}}{l_O}\right), \tag{8.1}$$

$$\boldsymbol{\nabla}_r \cdot (\overline{\boldsymbol{\delta u}'|\boldsymbol{\delta u}'|^2}) = \frac{V_{O3}^3(\boldsymbol{X})}{l_O} f_{O3}\left(\frac{\boldsymbol{r}}{l_O}\right), \tag{8.2}$$

$$2\boldsymbol{\nabla}_X \cdot \overline{(\boldsymbol{\delta u}'\delta p')} = \frac{V_{Op}^3(\boldsymbol{X})}{l_O} f_{Op}\left(\frac{\boldsymbol{r}}{l_O}\right). \tag{8.3}$$

Inner similarity for $|\boldsymbol{r}| \ll l_O$:

$$\boldsymbol{\nabla}_X \cdot (\overline{\boldsymbol{u}_{X'}|\boldsymbol{\delta u}'|^2}) = \frac{V_{IX}^3(\boldsymbol{X})}{l_I} f_{IX}\left(\frac{\boldsymbol{r}}{l_I}\right), \tag{8.4}$$

$$\boldsymbol{\nabla}_r \cdot (\overline{\boldsymbol{\delta u}'|\boldsymbol{\delta u}'|^2}) = \frac{V_{I3}^3(\boldsymbol{X})}{l_I} f_{I3}\left(\frac{\boldsymbol{r}}{l_I}\right), \tag{8.5}$$

$$2\boldsymbol{\nabla}_X \cdot \overline{(\boldsymbol{\delta u}'\delta p')} = \frac{V_{Ip}^3(\boldsymbol{X})}{l_I} f_{Ip}\left(\frac{\boldsymbol{r}}{l_I}\right). \tag{8.6}$$

The characteristic velocities $V_{OX}, V_{O3}, V_{Op}, V_{IX}, V_{I3}, V_{Ip}$ depend explicitly on $\boldsymbol{X}$ but are independent of $\boldsymbol{r}$ and $f_{OX}, f_{O3}, f_{Op}, f_{IX}, f_{I3}, f_{Ip}$ are dimensionless functions which do not depend explicitly on $\boldsymbol{X}$ within the similarity region. Statistical homogeneity is the special case where $f_{OX} = f_{Op} = f_{IX} = f_{Ip} = 0$ and the characteristic velocities are independent of $\boldsymbol{X}$.

As in the previous section, we expect the outer characteristic velocities to be independent of viscosity but the inner characteristic velocities to depend on it. The ratios of outer to inner characteristic velocities are therefore functions of local Reynolds number Re_O, i.e. $V_{IX}/V_{OX} = g_X(Re_O, \boldsymbol{X})$, $V_{I3}/V_{O3} = g_3(Re_O, \boldsymbol{X})$, $V_{Ip}/V_{Op} = g_p(Re_O, \boldsymbol{X})$, these functions approaching zero as Re_O tends to infinity.

Following the approach we took in § 7, we can replace the hypothesis of similarity by a hypothesis of isotropic similarity for terms on the left-hand side of (6.1). For the two terms not involving pressure fluctuations, this refined hypothesis states that

$$\frac{\partial}{\partial r_i}\overline{u'_{Xi}(\delta u'_j)^2} \quad \text{and} \quad \frac{\partial}{\partial r_i}\overline{\delta u'_i(\delta u'_j)^2} \tag{8.7a,b}$$

(without summation over i and without summation over j) have an inner and an outer similarity form for every $i, j = 1, 2, 3$. Only $i, j = 1, 3$ are accessible to our 2D2C PIV measurements and we therefore decompose the interscale transfer rate in two subterms, both of which have an inner and an outer similarity form:

$$\frac{\partial}{\partial r_x}\overline{[\delta u'_x(\delta u'^2_x + \delta u'^2_z)]} + \frac{\partial}{\partial r_z}\overline{[\delta u'_z(\delta u'^2_x + \delta u'^2_z)]} \equiv \boldsymbol{\nabla}_r \cdot \widetilde{(\boldsymbol{\delta u}'|\boldsymbol{\delta u}'|^2)} \tag{8.8}$$

which is accessible to our 2D2C PIV and

$$\frac{\partial}{\partial r_x}\overline{[\delta u'_x(\delta u'^2_y)]} + \frac{\partial}{\partial r_z}\overline{[\delta u'_z(\delta u'^2_y)]} + \frac{\partial}{\partial r_y}\overline{[\delta u'_y(\delta u'^2_x + \delta u'^2_y + \delta u'^2_z)]} \tag{8.9}$$

which is not. For example,

$$\boldsymbol{\nabla}_{\boldsymbol{r}} \cdot \widetilde{(\overline{\boldsymbol{\delta u}'|\boldsymbol{\delta u}'|^2})} = \frac{V_{O3}^3(\boldsymbol{X})}{l_O} F_{O3}\left(\frac{\boldsymbol{r}}{l_O}\right) \tag{8.10}$$

for $|\boldsymbol{r}| \gg l_I$ and

$$\boldsymbol{\nabla}_{\boldsymbol{r}} \cdot \widetilde{(\overline{\boldsymbol{\delta u}'|\boldsymbol{\delta u}'|^2})} = \frac{V_{I3}^3(\boldsymbol{X})}{l_I} F_{I3}\left(\frac{\boldsymbol{r}}{l_I}\right) \tag{8.11}$$

for $|\boldsymbol{r}| \ll l_O$. The function F_{O3} is not the same as the function f_{O3} and the function F_{I3} is not the same as the function f_{I3}.

We do the same for the interspace transfer rate $\boldsymbol{\nabla}_{\boldsymbol{X}} \cdot (\overline{\boldsymbol{u}_{\boldsymbol{X}}'|\boldsymbol{\delta u}'|^2})$ which we also decompose in two subterms, both of which have an inner and an outer similarity form. For the subterm which is accessible to our 2D2C PIV, for example

$$\frac{\partial}{\partial X_x}\overline{[u'_{Xx}(\delta u_x'^2 + \delta u_z'^2)]} + \frac{\partial}{\partial X_z}\overline{[u'_{Xz}(\delta u_x'^2 + \delta u_z'^2)]} \equiv \boldsymbol{\nabla}_{\boldsymbol{X}} \cdot \widetilde{(\overline{\boldsymbol{u}_{\boldsymbol{X}}'|\boldsymbol{\delta u}'|^2})}, \tag{8.12}$$

we therefore write

$$\boldsymbol{\nabla}_{\boldsymbol{X}} \cdot \widetilde{(\overline{\boldsymbol{u}_{\boldsymbol{X}}'|\boldsymbol{\delta u}'|^2})} = \frac{V_{OX}^3(\boldsymbol{X})}{l_O} F_{OX}\left(\frac{\boldsymbol{r}}{l_O}\right) \tag{8.13}$$

for $|\boldsymbol{r}| \gg l_I$ and

$$\boldsymbol{\nabla}_{\boldsymbol{X}} \cdot \widetilde{(\overline{\boldsymbol{u}_{\boldsymbol{X}}'|\boldsymbol{\delta u}'|^2})} = \frac{V_{IX}^3(\boldsymbol{X})}{l_I} F_{IX}\left(\frac{\boldsymbol{r}}{l_I}\right) \tag{8.14}$$

for $|\boldsymbol{r}| \ll l_O$. Again, the function F_{OX} is not the same as the function f_{OX} and the function F_{IX} is not the same as the function f_{IX}.

8.1. *Outer balance*

Using the outer similarity forms (8.1), (8.2) and (8.3), Chen & Vassilicos (2022) have shown that the outer form of the small-scale energy balance (6.1) for $|\boldsymbol{r}| \gg l_I$ tends to

$$\frac{V_{OX}^3}{V_{O2}^3} f_{OX}(\boldsymbol{r}/l_O) + \frac{V_{O3}^3}{V_{O2}^3} f_{O3}(\boldsymbol{r}/l_O) + \frac{V_{Op}^3}{V_{O2}^3} f_{Op}(\boldsymbol{r}/l_O) = -C_\epsilon \tag{8.15}$$

as $Re_O \to \infty$, where the dissipation coefficient C_ϵ is defined on the basis of the turbulence dissipation scaling $\overline{\epsilon'} \sim V_{O2}^3/l_O$. This scaling follows from the hypothesis (often referred to as zeroth law of turbulence) that the turbulence dissipation rate is independent of the fluid's viscosity at large enough Reynolds number, hence $\overline{\epsilon'} = C_\epsilon V_{O2}^3/l_O$, where C_ϵ is independent of Reynolds number but can depend on $\boldsymbol{X}$ and boundary/forcing conditions. It follows from (8.15) that

$$V_{OX} \sim V_{O3} \sim V_{Op} \sim C_\epsilon^{1/3} V_{O2} \tag{8.16}$$

which means that all three velocities V_{OX}, V_{O3} and V_{Op} are the same function of $\boldsymbol{X}$ as $C_\epsilon^{1/3} V_{O2}$. The independence of C_ϵ on $\boldsymbol{r}$ which is required to go from (8.15) to (8.16) is valid without any restriction on spatial gradients of turbulent dissipation: the only requirement is that the second-order spatial derivative of turbulent dissipation should be small compared with $\overline{\epsilon'}/l_O^2$.

8.2. *Inner balance*

Using the inner similarity forms (8.4), (8.5) and (8.6), Chen & Vassilicos (2022) have shown that the inner form of the small-scale energy balance (6.1) for $|\boldsymbol{r}| \ll l_O$ tends to

$$g_X^3 g_l^{-1} f_{IX}(\boldsymbol{r}/l_I) + g_3^3 g_l^{-1} f_{I3}(\boldsymbol{r}/l_I) + g_p^3 g_l^{-1} f_{Ip}(\boldsymbol{r}/l_I) = -1 + C_\epsilon^{-1} Re_O^{-1} g_2^2 g_l^{-2} \boldsymbol{\nabla}^2_{\boldsymbol{r}/l_I} f_{I2}(\boldsymbol{r}/l_I) \tag{8.17}$$

as $Re_O \to \infty$, where $\boldsymbol{\nabla}^2_{\boldsymbol{r}/l_I}$ is the Laplacian with respect to $\boldsymbol{r}/l_I$ and where $Re_O^{-1} g_2^2 g_l^{-2}$ is independent of Reynolds number. They obtained this result without considering the possibility of explicit dependencies of the functions g_X, g_3, g_p, g_l on $\boldsymbol{X}$ but it can be checked that their result remains intact if such dependencies are taken into account. Writing

$$g_2^2(Re_O, \boldsymbol{X}) g_l^{-2}(Re_O, \boldsymbol{X}) = A_3(\boldsymbol{X}) Re_O \tag{8.18}$$

in terms of a dimensionless coefficient A_3 which can depend on $\boldsymbol{X}$ (but not on $\boldsymbol{r}$ and viscosity), we note that (8.17) is viable only if $g_X^3 g_l^{-1}$, $g_3^3 g_l^{-1}$, $g_p^3 g_l^{-1}$ and A_3/C_ϵ are all independent of $\boldsymbol{X}$. Incidentally, the explicit $\boldsymbol{X}$ dependence of the functions g_2 and g_l and the constraint $A_3/C_\epsilon = $ const. independent of $\boldsymbol{X}$ cancel the need for the theoretical readjustments in the Appendix of Chen & Vassilicos (2022).

With (7.6) and the exponent $n = 2/3$ obtained theoretically in § 7, (8.18) implies $g_l \sim Re_O^{-3/4}$, therefore

$$l_I \sim l_O Re_O^{-3/4}, \tag{8.19}$$

where the coefficient of proportionality can, in principle, be a function of $\boldsymbol{X}$. Using (8.18) once again leads to

$$V_{I2} \sim V_{O2} Re_O^{-1/4}, \tag{8.20}$$

where the coefficient of proportionality is also, in principle, a function of $\boldsymbol{X}$. One notes the resemblance of l_I and V_{I2} with the Kolmogorov length and velocity scales. In fact, they depend on viscosity in exactly the same way that the corresponding Kolmogorov scales depend on viscosity (see Chen & Vassilicos (2022) for more on this comparison). However, these forms of l_I and V_{I2} have been obtained from $n = 2/3$ and the inner form of the small-scale energy budget (i.e. effectively from our similarity assumptions and the Navier–Stokes equation) in an explicitely non-homogeneous context with hypotheses which, unlike those of Kolmogorov (see Frisch (1995), Pope (2000) and § 2 of Chen & Vassilicos (2022)), are adapted to non-homogeneous non-equilibrium turbulence. Note, in passing, that the sole purpose for which the value 2/3 of the exponent n is used in this paper is to derive (8.19) and (8.20), nothing else, and that (8.19) and (8.20) are not used to derive anything in the paper either.

8.3. *Intermediate scalings*

The turbulence dissipation scaling $\overline{\epsilon'} = C_\epsilon V_{O2}^3/l_O$ and (8.16) imply

$$\overline{\epsilon'} \sim V_{O3}^3/l_O \sim V_{OX}^3/l_O \sim V_{Op}^3/l_O, \tag{8.21}$$

where the proportionality coefficients are independent of $\boldsymbol{X}$ (and of course also independent of Re_O). One expects the nonlinear terms to be part of the small-scale energy balance (8.17) which means that $g_X^3 g_l^{-1}$, $g_3^3 g_l^{-1}$ and $g_p^3 g_l^{-1}$ should be independent of Re_O

in the limit $Re_O \to \infty$ and so we write, in this limit, $g_X^3 g_l^{-1} = B_X$, $g_3^3 g_l^{-1} = B_3$ and $g_p^3 g_l^{-1} = B_p$, where the dimensionless constants B_X, B_3, B_p are independent of $\boldsymbol{X}$, $\boldsymbol{r}$ and Re_O. With (8.21), the implication is

$$\overline{\epsilon'} \sim V_{I3}^3/l_I \sim V_{IX}^3/l_I \sim V_{Ip}^3/l_I, \tag{8.22}$$

where, once again, the proportionality coefficients are independent of $\boldsymbol{X}$ and Re_O. The inner–outer equivalence hypothesis (8.22) of Chen & Vassilicos (2022) for turbulence dissipation is derived here from a more intuitively natural hypothesis. Hence, in the intermediate range $l_I \ll |\boldsymbol{r}| \ll l_O$ where (8.1) matches (8.4), (8.2) matches (8.5) and (8.3) matches (8.6), we get $f_{OX}(\boldsymbol{r}/l_O) = B_X f_{IX}(\boldsymbol{r}/l_I)$, $f_{O3}(\boldsymbol{r}/l_O) = B_3 f_{I3}(\boldsymbol{r}/l_I)$ and $f_{Op}(\boldsymbol{r}/l_O) = B_p f_{Ip}(\boldsymbol{r}/l_I)$. These functions are therefore asymptotic constants in the intermediate range $l_I \ll |\boldsymbol{r}| \ll l_O$ as $Re_O \to \infty$, and, therefore,

$$\boldsymbol{\nabla}_X \cdot (\overline{\boldsymbol{u}_{X'} |\boldsymbol{\delta u'}|^2}) \sim \overline{\epsilon'}, \tag{8.23}$$

$$\boldsymbol{\nabla}_{\boldsymbol{r}} \cdot (\overline{\boldsymbol{\delta u'} |\boldsymbol{\delta u'}|^2}) \sim \overline{\epsilon'} \tag{8.24}$$

and

$$2\boldsymbol{\nabla}_X \cdot \overline{(\boldsymbol{\delta u'} \delta p')} \sim \overline{\epsilon'} \tag{8.25}$$

in that range.

The dimensionless coefficients of proportionality in (8.23), (8.24) and (8.25) are independent of $\boldsymbol{r}$, independent of Reynolds number and independent of $\boldsymbol{X}$ in the similarity region of the flow considered. They add up to -1 asymptotically as $Re_O \to \infty$. These equations reflect a situation where the cascade is not impermeable in the sense that turbulence energy is lost/transferred to neighbouring physical space at any scale where it is also cascaded. Equally, these equations reflect a situation where turbulence energy is being cascaded and thereby dissipated while it spreads in physical space, thereby preventing spatial homogenisation (as shown by Alexakis 2023) at all scales where this happens. In fact recent investigations reveal that interscale and interspace transfer rates are coupled and/or correlated in various cases of non-homogeneity: see figure 2 in Zhou & Vassilicos (2020) and their related discussion concerning energy transfers at the turbulent–non-turbulent interface; see figure 15 in Larssen & Vassilicos (2023) and their related discussion concerning local fluctuating inhomogeneities in periodic turbulence. (The paper by Larssen & Vassilicos (2023) and the papers by Alves Portela *et al.* (2017) and Alves Portela, Papadakis & Vassilicos (2020) also report intimate links between interscale transfer and pressure–velocity correlations.)

The same procedure applied to (8.10) and (8.11) on the one hand and to (8.13) and (8.14) on the other yields

$$\boldsymbol{\nabla}_X \cdot \widetilde{(\overline{\boldsymbol{u}_{X'} |\boldsymbol{\delta u'}|^2})} \sim \overline{\epsilon'} \tag{8.26}$$

and

$$\boldsymbol{\nabla}_{\boldsymbol{r}} \cdot \widetilde{(\overline{\boldsymbol{\delta u'} |\boldsymbol{\delta u'}|^2})} \sim \overline{\epsilon'} \tag{8.27}$$

in the intermediate range $l_I \ll |\boldsymbol{r}| \ll l_O$ as $Re_O \to \infty$. The dimensionless coefficients of proportionality in these two relations are also independent of $\boldsymbol{r}$, Reynolds number and $\boldsymbol{X}$.

Note that our analysis does not reveal the signs of the various constants of proportionality in the five proportionality relations above. These signs are important, in particular for the interscale transfer rate as its sign can discriminate between transfer

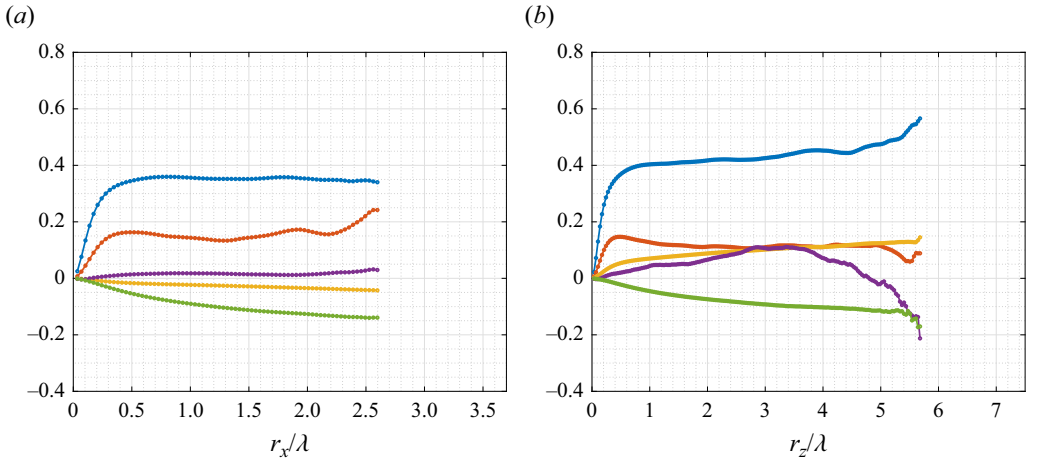

Figure 10. Truncation estimates of the measured energy terms in (2.4) normalised by the dissipation $\langle\overline{\epsilon'}\rangle$ for one configuration (fractal blades at 1 Hz). Blue: $\langle\nabla_{\boldsymbol{r}}\cdot\widetilde{(\overline{\delta\boldsymbol{u}'|\delta\boldsymbol{u}'|^2})}\rangle$; red: $\langle\nabla_{\boldsymbol{X}}\cdot\widetilde{(\overline{\boldsymbol{u}_{\boldsymbol{X}}'|\delta\boldsymbol{u}'|^2})}\rangle$; green: $2\widetilde{P}_r+2\widetilde{P^s_{Xr}}$; yellow: $\langle\widetilde{\delta\bar{\boldsymbol{u}}\cdot\nabla_{\boldsymbol{r}}\overline{|\delta\boldsymbol{u}'|^2}}\rangle$; purple: $\langle\widetilde{\overline{\boldsymbol{u}_{\boldsymbol{X}}}\cdot\nabla_{\boldsymbol{X}}\overline{|\delta\boldsymbol{u}'|^2}}\rangle$. (*a*) The r_x direction. (*b*) The r_z direction.

from small to large scales (forward cascade) or from large to small scales (inverse cascade). The last two proportionalities are the ones which are accessible to our 2D2C PIV measurements. For them, our measurements can establish whether the proportionality constants are well defined and, if they are, whether they are negative or positive.

Before moving to our energy transfer measurements, we note that the hypothesis of inner–outer equivalence for turbulence dissipation introduced by Chen & Vassilicos (2022) and used in § 7 can now be seen to be a consequence of Reynolds-number independence of turbulence dissipation, outer and inner similarities and the natural assumption $V_{I3}=C_I(\boldsymbol{X})V_{I2}$, where the dimensionless coefficient $C_I(\boldsymbol{X})$ is independent of Re_O and $\boldsymbol{r}$. Using $\overline{\epsilon'}=C_\epsilon(\boldsymbol{X})V_{O2}^3/l_O$ and the first proportionality in (8.22) (which follows from inner and outer similarities and the Navier–Stokes two-point energy balance), one then obtains the inner–outer equivalence in the form $C_\epsilon(\boldsymbol{X})V_{O2}^3/l_O\sim C_I^3(\boldsymbol{X})V_{I2}^3/l_I$ with a proportionality coefficient that is independent of $\boldsymbol{X}$ and Re_O. (It also follows that $C_\epsilon(\boldsymbol{X})/C_I^3(\boldsymbol{X})$ is independent of $\boldsymbol{X}$.)

8.4. *Energy transfer rate measurements*

The quantities obtained from our 2D2C PIV and presented in this subsection require high spatial resolution, in particular for the estimation of the turbulence dissipation rate, and a high number of samples for convergence of third-order statistics. Averaging over time is not enough for such convergence (see § 4 of the supplementary material). We therefore calculate spatial averages of all (already time-averaged) truncated terms in (2.4). In figure 10 we plot a representative example of these terms for the fractal blade $F=1$ Hz configuration. Even though the two-point turbulence production rate is not negligible, the theory's predictions concerning the constancy in r_x and r_z of the normalised interspace and interscale energy transfer rates seem to hold. Some of the small-scale linear transport terms are not negligible either but this has no bearing on the theory which leads to the same conclusions if taken explicitly into account (see Chen & Vassilicos 2022).

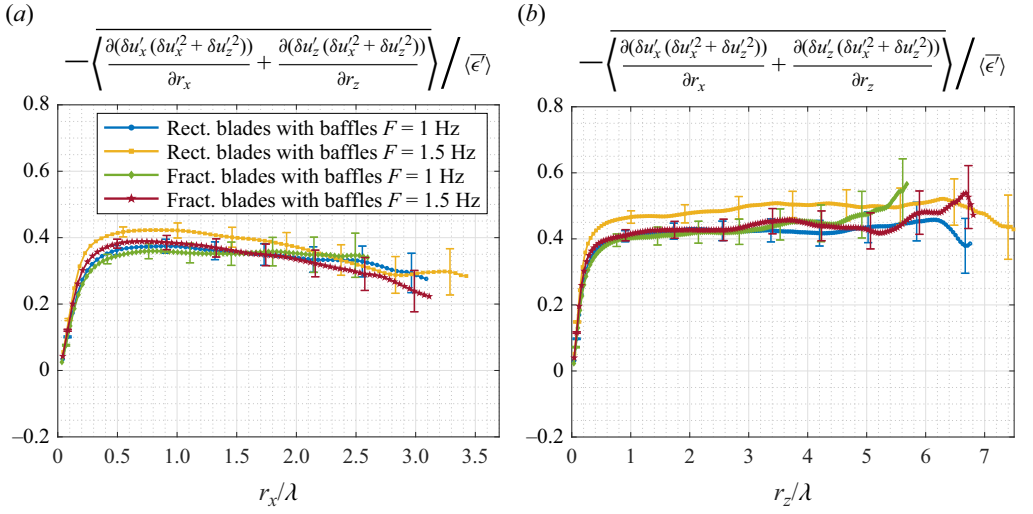

Figure 11. Interscale transfer rate estimate. (*a*) The r_x direction. (*b*) The r_z direction.

We now look in more detail at the spatial averages of both sides of proportionalities (8.26) and (8.27) given that they are the consequences of our theory that can be tested by our 2D2C PIV. In figures 11 and 12 we plot the normalised interscale transfer rate term $\boldsymbol{\nabla_r \cdot \langle \widetilde{\delta u' |\delta u'|^2} \rangle / \langle \overline{\epsilon'} \rangle}$ and the normalised interspace transfer rate term $\boldsymbol{\nabla_X \cdot \langle \widetilde{u_X' |\delta u'|^2} \rangle / \langle \overline{\epsilon'} \rangle}$ (we recall that the angle brackets represent averages over $\boldsymbol{X}$ in the plane of our field of view). Our theory predicts that an intermediate range of scales exists where these two normalised terms are about constant, this constant being the same for different Reynolds numbers. The spread of Taylor-length-based Reynolds numbers across our four experimental configurations is from 480 to 650, and the average turbulence dissipation rate varies by a factor of 4 across these configurations. The Taylor length λ depends on the turbulence dissipation rate and in §§ 1.1 and 1.2 of the supplementary material we explain how we calculate both of them and how we denoise the PIV data for this purpose. The value of the average turbulence dissipation rate is probably slightly underestimated and this uncertainty is not taken into account in the error bars shown in figures 11 and 12. The spatial resolutions for all four configurations are given in table 1.

The normalised energy transfer terms are plotted versus r_x/λ in figures 11(*a*) and 12(*a*) and versus r_z/λ in figures 11(*b*) and 12(*b*). We normalise the components r_x and r_z of the vector $\boldsymbol{r}$ by λ because of the important role that λ has been shown to play in the separation length scale dependence of the interscale transfer rate in decaying homogeneous turbulence (Obligado & Vassilicos 2019; Meldi & Vassilicos 2021) and in fully developed turbulent channel flow (Apostolidis *et al.* 2023). We find (figure 11) that the interscale transfer rate is negative for all observed scales in both directions r_x and r_z and all four configurations. This suggests a nonlinear interscale turbulent energy transfer that is predominantly from large to small scales, i.e. that the turbulence cascade is forward on average. The 2D2C PIV measurements also appear to support our theory's prediction that a range of scales exists where the interscale transfer rate is proportional to the turbulence dissipation rate and independent of two-point separation length. Indeed, for the four configurations, $\boldsymbol{\nabla_r \cdot \langle \widetilde{\delta u' |\delta u'|^2} \rangle / \langle \overline{\epsilon'} \rangle}$ appears to collapse within error bars around a constant value between 0.35 and 0.45 in the range $\lambda/2 \leq r_x \leq 2\lambda$ and around a constant

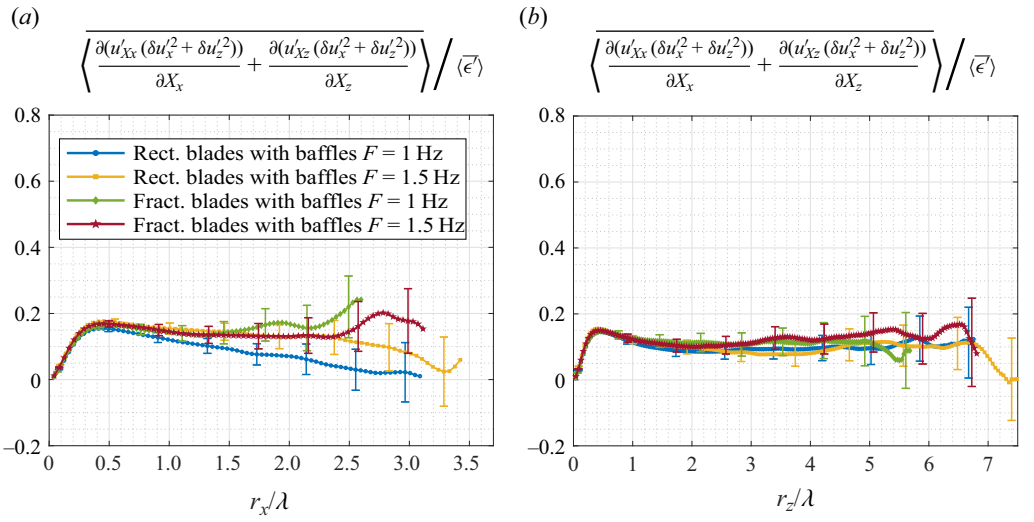

Figure 12. Interspace transport rate estimate. (*a*) The r_x direction. (*b*) The r_z direction.

value between 0.4 and 0.5 in the range $\lambda/2 \leq r_z \leq 5\lambda$. Beyond these values of r_x and r_z statistical convergence visibly weakens. The Taylor length takes values between 3.7 and 4.9 mm across our four configurations and the field of view of our PIV is 27 mm $\times$ 28 mm, hence we cannot access values of r_x/λ and r_z/λ larger than those in the plots of figures 11 and 12 (to avoid symmetry problems, we only used the right half of our field of view in the x direction).

Whilst the negative sign of the average interscale transfer rate and its proportionality with the average turbulence dissipation rate over a range of scales are similar to Kolmogorov's prediction for the average interscale transfer rate in high-Reynolds-number statistically homogeneous stationary turbulence (Frisch (1995), Pope (2000) and § 2 of Chen & Vassilicos (2022)), the constant of proportionality is not -1 as in Kolmogorov equilibrium but significantly smaller in magnitude. This difference may of course be accounted for by the difference between $\boldsymbol{\nabla}_{\boldsymbol{r}} \cdot \langle \overline{\boldsymbol{\delta u}'|\boldsymbol{\delta u}'|^2} \rangle / \langle \overline{\epsilon}' \rangle$ and $\boldsymbol{\nabla}_{\boldsymbol{r}} \cdot (\langle \overline{\boldsymbol{\delta u}'|\boldsymbol{\delta u}'|^2} \rangle) / \langle \overline{\epsilon}' \rangle$ and/or the Reynolds number not being large enough in the case that this constant of proportionality has finite-Reynolds-number corrections. However, the results in figures 12(*a*) and 12(*b*) make it clear that the turbulence studied here is significantly non-homogeneous at the scales where $\boldsymbol{\nabla}_{\boldsymbol{r}} \cdot \langle \overline{\boldsymbol{\delta u}'|\boldsymbol{\delta u}'|^2} \rangle / \langle \overline{\epsilon}' \rangle$ is about constant. Indeed, these figures show that the normalised interspace transfer rate term $\boldsymbol{\nabla}_{\boldsymbol{X}} \cdot \langle \overline{\boldsymbol{u}_{\boldsymbol{X}}'|\boldsymbol{\delta u}'|^2} \rangle / \langle \overline{\epsilon}' \rangle$ is very significantly non-zero and in fact positive over all accessible length scales in both directions r_x and r_z for all four configurations. These consistent positive values mean that there is an average turbulent flux which takes small-scale turbulent kinetic energy out of the field of view at all accessible length scales.

For all four configurations, $\boldsymbol{\nabla}_{\boldsymbol{X}} \cdot \langle \overline{\boldsymbol{u}_{\boldsymbol{X}}'|\boldsymbol{\delta u}'|^2} \rangle / \langle \overline{\epsilon}' \rangle$ appear to collapse within error bars around a constant value between about 0.05 and 0.15 in the range $\lambda/2 \leq r_x \leq 2\lambda$ and around a similar constant value in the range $\lambda/2 \leq r_z \leq 5\lambda$ (see figure 12*a*,*b*). We stress once again that larger two-point separation scales are not accessible to our PIV and statistical convergence weakens at the larger values of r_x and r_z that we can access. Nevertheless, the results in figures 12(*a*) and 12(*b*) do not invalidate and may even arguably

offer some support to our theory's prediction (8.26) for the interspace turbulence transfer rate.

To summarise, the parts of the interscale and of the interspace average turbulent transfer rates that we can access appear to be independent of two-point separation scale and are proportional to the average turbulence dissipation rate over a more or less overlapping range of scales. The average turbulence dissipation rate and the Taylor length scale collapse the two-point separation scale dependence of the accessible parts of the energy transfer rates for all four configurations tried here.

The average interscale transfer rate is negative, suggesting forward cascade, and the average interspace transfer rate is positive, suggesting outward turbulent transport of small-scale turbulence. This outward spatial turbulent flux is overwhelmingly in the x direction. The non-homogeneity that it represents is present even at the smallest scales of the turbulence, in particular scales between $\lambda/2$ and 5λ. It is therefore not possible to apply the Kolmogorov equilibrium theory to the small scales of the present turbulent flows. However, our non-equilibrium theory of non-homogeneous small-scale turbulence is able to account for some of our observations.

One can also analyse subterms of the parts of the average interscale transfer rate and interspace transport rate that we measure. These results are presented in Appendix A where we report that they are constant over the range of scales where their sum is constant.

The magnitude of the accessible average interscale transfer rate is roughly four times larger than the magnitude of the accessible average interspace transfer rate. Considering our measurements, our theory (in particular (8.25)) and the small-scale energy balance (6.1) averaged over the field of view of our PIV, it is highly likely that the pressure–velocity term in that balance plays a dominant role at scales $|\boldsymbol{r}|$ larger than $\lambda/2$.

9. Large-scale turbulent energy budget

We do not apply the previous section's theoretical approach to the large-scale turbulent energy budget, (2.8), given that the two-point turbulence production rate P_X tends to the one-point turbulence production rate in the limit $\boldsymbol{r} \to 0$ and given the PIV evidence of § 5 suggesting that it is significantly non-zero at the smallest scales and does not collapse with the average turbulence dissipation rate. Indeed, the results for P_X presented in the supplementary material show that $\langle \widetilde{\overline{P_X}} \rangle / \langle \overline{\epsilon'} \rangle$ differs substantially for the regular and the fractal-like blades.

Furthermore, the spatio-temporal average of the part of the interspace turbulent transport rate of large-scale turbulence energy that is accessible to our 2D2C PIV, i.e.

$$\frac{\partial}{\partial X_x} \langle \overline{[u'_{Xx}(u'^2_{Xx} + u'^2_{Xz})]} \rangle / \langle \overline{\epsilon'} \rangle + \frac{\partial}{\partial X_z} \langle \overline{[u'_{Xz}(u'^2_{Xx} + u'^2_{Xz})]} \rangle \equiv \langle \boldsymbol{\nabla}_{\boldsymbol{X}} \cdot \widetilde{(\overline{\boldsymbol{u}_{\boldsymbol{X}'} |\boldsymbol{u}_{\boldsymbol{X}'}|^2})} \rangle, \tag{9.1}$$

does not collapse with the average turbulence dissipation rate $\langle \overline{\epsilon'} \rangle$. This is clear in figure 13 which also shows that the normalised spatio-temporal average $\langle \boldsymbol{\nabla}_{\boldsymbol{X}} \cdot \widetilde{(\overline{\boldsymbol{u}_{\boldsymbol{X}'} |\boldsymbol{u}_{\boldsymbol{X}'}|^2})} \rangle / \langle \overline{\epsilon'} \rangle$ may depend linearly on r_z for $r_z \geq \lambda/2$ and may be constant or linear with r_x for $r_x \geq \lambda/2$ depending on the type of blade. This is very different behaviour from that of the average interspace turbulent transport rate of small-scale energy in figure 12.

Another important difference is the non-vanishing value when $\boldsymbol{r} \to 0$ of the average interspace turbulent transport rate of large-scale energy (see figure 13). Indeed, when $\boldsymbol{r} \to 0$, this term converges to the space–time averaged one-point turbulent energy transport rate $\langle \overline{\boldsymbol{\nabla} \cdot \boldsymbol{u}' |\boldsymbol{u}'|^2} \rangle$. This one-point turbulence transport rate reflects the non-homogeneity

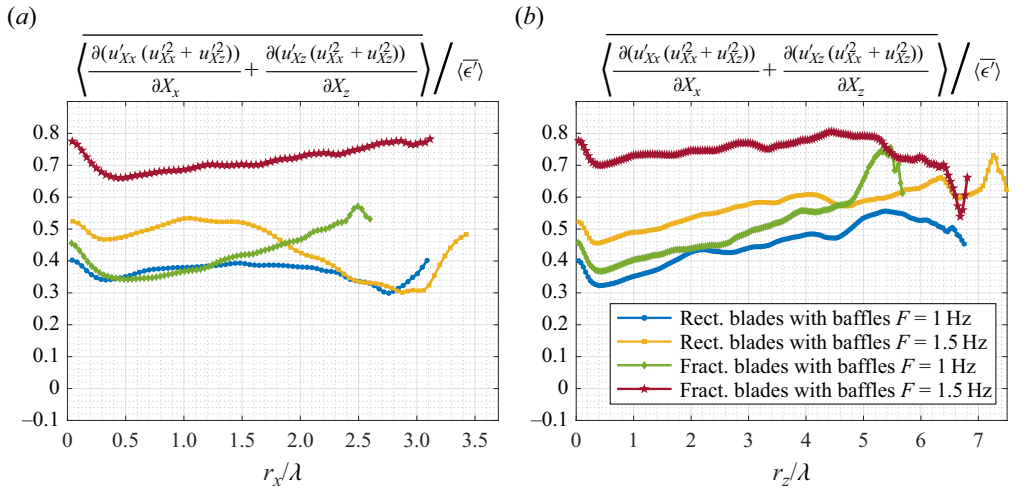

Figure 13. Interspace transfer estimate of $\boldsymbol{u_X}^2$. (*a*) The r_x direction. (*b*) The r_z direction.

of each particular configuration and there is no reason to expect it to collapse when normalised by dissipation. There is therefore no reason either to expect such a collapse for the average two-point interspace turbulent transport rate of large-scale energy at the smallest two-point separations. Consistently, the measurements suggest that such a collapse is in fact absent at all two-point separations tested (figure 13).

The indications are, therefore, that the large-scale turbulent energy budget (2.8) is very different from the small-scale turbulent energy budget and that a theory of the type developed in the previous section for the small-scale turbulent energy budget cannot be developed for the large-scale turbulent energy budget. Nevertheless, there is a kinematic relation between the rate with which large scales gain or lose turbulent energy to the small scales via nonlinear turbulence interactions and the rate with which small scales gain or lose turbulent energy via such interactions. This is (3.2). Neglecting mean flow velocity differences and two-point turbulence production rates P_r and P^I_{Xr}, as appears to be possible in our PIV's field of view for small two-point separation lengths, (3.2) becomes

$$\boldsymbol{\nabla_r}\cdot(\overline{\boldsymbol{\delta u'}|\boldsymbol{\delta u'}|^2})+\boldsymbol{\nabla_r}\cdot(\overline{\boldsymbol{\delta u'}|\boldsymbol{u_X}'|^2})=2\boldsymbol{\nabla_X}\cdot(\overline{\boldsymbol{\delta u'}(\boldsymbol{\delta u'}\cdot\boldsymbol{u'_X})}), \tag{9.2}$$

where $\boldsymbol{\nabla_r}\cdot(\overline{\boldsymbol{\delta u'}|\boldsymbol{u_X}'|^2})$ represents the rate with which large scales lose or gain turbulent energy to or from the small scales and $\boldsymbol{\nabla_r}\cdot(\overline{\boldsymbol{\delta u'}|\boldsymbol{\delta u'}|^2})$ represents the rate with which small scales gain or lose turbulent energy by the nonlinear turbulence interactions (see also the complementary description of these transfer rates under (3.2)). In general, and in the present flow in particular, the passage of turbulent energy from large to small scales (or vice versa) is not necessarily 'impermeable' as energy can leak out of this cascade process because of non-homogeneities, in the present case by the spatial gradient term on the right-hand side of (9.2).

In figure 14 we plot the spatio-temporal average of the part of $\boldsymbol{\nabla_r}\cdot(\overline{\boldsymbol{\delta u'}|\boldsymbol{u_X}'|^2})$ that is accessible to our 2D2C PIV, namely

$$\frac{\partial}{\partial r_x}\langle\overline{[\delta u'_x(u'^2_{Xx}+u'^2_{Xz})]}\rangle+\frac{\partial}{\partial r_z}\langle\overline{[\delta u'_z(u'^2_{Xx}+u'^2_{Xz})]}\rangle\equiv\langle\boldsymbol{\nabla_r}\cdot\widetilde{(\overline{\boldsymbol{\delta u'}|\boldsymbol{u_X}'|^2})}\rangle. \tag{9.3}$$

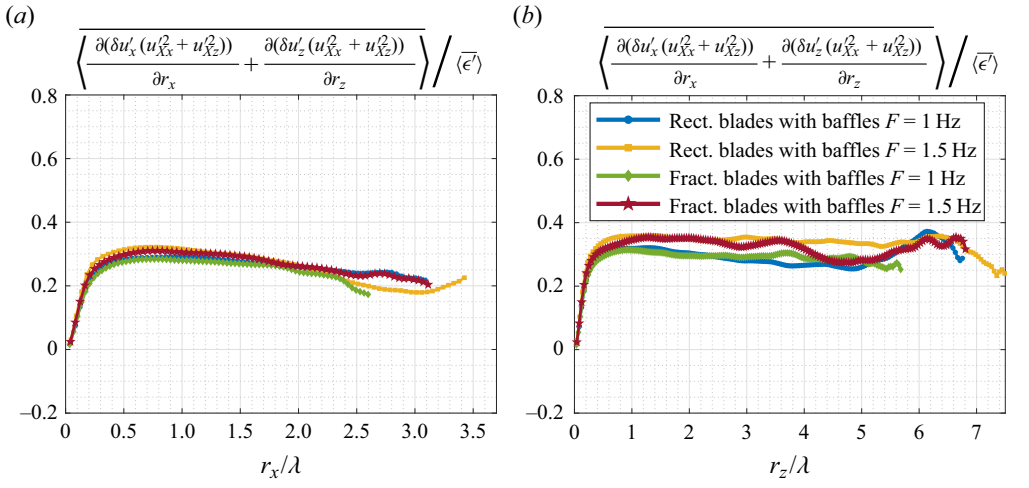

Figure 14. Interscale transfer estimate of $\boldsymbol{u_X}^2$. (*a*) The r_x direction. (*b*) The r_z direction.

We plot it normalised by $\langle\overline{\epsilon'}\rangle$ versus both r_x/λ and r_z/λ and we note that it collapses well for the four different configurations. Furthermore, it appears to have a constant value across the same ranges $\lambda/2 \leq r_x \leq 2\lambda$ and $\lambda/2 \leq r_z \leq 5\lambda$ where the part of the spatio-temporal average of $\boldsymbol{\nabla_r} \cdot (\overline{\boldsymbol{\delta u'}|\boldsymbol{\delta u'}|^2})$ that is accessible to our PIV has an approximately collapsed constant value (figure 11). This suggests a strong link between these two turbulent energy transfer rates.

The positive constant value of $\langle \boldsymbol{\nabla_r} \cdot (\overline{\boldsymbol{\delta u'}|\boldsymbol{u_X}'|^2}) \rangle / \langle\overline{\epsilon'}\rangle$ (see figure 14) is slightly lower than the magnitude of the negative constant value of $\boldsymbol{\nabla_r} \cdot \langle\overline{\boldsymbol{\delta u'}|\boldsymbol{\delta u'}|^2}\rangle / \langle\overline{\epsilon'}\rangle$ (see figure 11). If this experimental observation reflects a similar difference between $\boldsymbol{\nabla_r} \cdot (\overline{\boldsymbol{\delta u'}|\boldsymbol{u_X}'|^2})$ and $\boldsymbol{\nabla_r} \cdot (\overline{\boldsymbol{\delta u'}|\boldsymbol{\delta u'}|^2})$ then the interpretation will have to be that large scales lose energy to small scales but that the small scales receive more of the energy lost by the large ones because some energy is transported from elsewhere in physical space without changing scale. In the kinematic equation (9.2), this energy leak away from the interscale turbulent energy transfer process is accounted for by $2\boldsymbol{\nabla_X} \cdot (\overline{\boldsymbol{\delta u'}(\boldsymbol{\delta u'} \cdot \boldsymbol{u'_X})})$ which can be non-zero in non-homogeneous turbulence (or, more generally, by all the other terms present in (3.2) if they cannot be neglected).

The experimental results presented in figure 14 may be reflecting a proportionality

$$\boldsymbol{\nabla_r} \cdot \langle \boldsymbol{\delta u'}|\boldsymbol{u_X}'|^2 \rangle \sim \langle \epsilon' \rangle \tag{9.4}$$

which cannot be confirmed or invalidated with our 2D2C PIV. This proportionality concerns interscale energy transfer within the large-scale turbulent energy budget and is additional to the proportionalities (8.23), (8.24), (8.25) obtained in the previous section on the basis of the small-scale turbulent energy budget. The previous section's theory does not give the proportionality coefficients of these relations. In the following section we present a hypothesis which has the power, if and when valid, to determine some such proportionality coefficients.

10. A local small-scale homogeneity hypothesis

We consider statistically stationary non-homogeneous turbulence by comparison with the case of statistically homogeneous non-stationary turbulence which we addressed in § 3 (equations (3.3) to (3.8)). Statistical stationarity is meant in the Lagrangian sense of following the mean flow, i.e. $\overline{\boldsymbol{u}_X}\cdot\boldsymbol{\nabla}_X\frac{1}{2}\overline{|\boldsymbol{\delta u'}|^2}=0=\overline{\boldsymbol{u}_X}\cdot\boldsymbol{\nabla}_X\frac{1}{2}\overline{|\boldsymbol{u'}_X|^2}$. This is indeed the case in the present flows because the mean flow velocity is vertical (i.e. in the z direction) and the turbulence varies mainly in the horizontal direction. With this statistical stationarity and by considering scales $|\boldsymbol{r}|$ large enough to neglect viscous diffusion, fluctuating energy equations (2.4) and (2.8) become, respectively,

$$\begin{aligned}&\boldsymbol{\delta\bar{u}}\cdot\boldsymbol{\nabla}_{\boldsymbol{r}}\frac{1}{2}\overline{|\boldsymbol{\delta u'}|^2}-P_r-P^s_{Xr}+\boldsymbol{\nabla}_X\cdot\left(\overline{\boldsymbol{u}_{X'}\frac{1}{2}|\boldsymbol{\delta u'}|^2}+\overline{\boldsymbol{\delta u'}\delta p'}\right)\\&\quad\approx-\boldsymbol{\nabla}_{\boldsymbol{r}}\cdot\left(\overline{\boldsymbol{\delta u'}\frac{1}{2}|\boldsymbol{\delta u'}|^2}\right)-\frac{\nu}{4}\overline{\frac{\partial u_i'^{+}}{\partial\zeta_k^{+}}\frac{\partial u_i'^{+}}{\partial\zeta_k^{+}}}-\frac{\nu}{4}\overline{\frac{\partial u_i'^{-}}{\partial\zeta_k^{-}}\frac{\partial u_i'^{-}}{\partial\zeta_k^{-}}}\end{aligned}\tag{10.1}$$

and

$$\begin{aligned}&\boldsymbol{\delta\bar{u}}\cdot\boldsymbol{\nabla}_{\boldsymbol{r}}\frac{1}{2}\overline{|\boldsymbol{u'}_X|^2}-P_X-P^l_{Xr}+\boldsymbol{\nabla}_X\cdot\left(\overline{\boldsymbol{u}_{X'}\frac{1}{2}|\boldsymbol{u}_{X'}|^2}+\overline{\boldsymbol{u}_{X'}p'_X}\right)\\&\quad\approx-\boldsymbol{\nabla}_{\boldsymbol{r}}\cdot\left(\overline{\boldsymbol{\delta u'}\frac{1}{2}|\boldsymbol{u}_{X'}|^2}\right)-\frac{\nu}{4}\overline{\frac{\partial u_i'^{+}}{\partial\zeta_k^{+}}\frac{\partial u_i'^{+}}{\partial\zeta_k^{+}}}-\frac{\nu}{4}\overline{\frac{\partial u_i'^{-}}{\partial\zeta_k^{-}}\frac{\partial u_i'^{-}}{\partial\zeta_k^{-}}}.\end{aligned}\tag{10.2}$$

We formulate a hypothesis of local homogeneity as a parallel to Kolmogorov's small-scale stationarity hypothesis (see § 3). Whereas most terms on the left-hand side of (10.2) do not tend to 0 as $\boldsymbol{r}$ tends to 0, the left-hand side of (10.1) does tend to 0 in that limit. The local small-scale homogeneity hypothesis that we make is the hypothesis that in the limit of increasing Reynolds number, the magnitude of $\boldsymbol{\delta\bar{u}}\cdot\boldsymbol{\nabla}_{\boldsymbol{r}}\frac{1}{2}\overline{|\boldsymbol{\delta u'}|^2}-P_r-P^s_{Xr}+\boldsymbol{\nabla}_X\cdot(\overline{\boldsymbol{u}_{X'}\frac{1}{2}|\boldsymbol{\delta u'}|^2}+\overline{\boldsymbol{\delta u'}\delta p'})$ is increasingly smaller than the local time-averaged turbulence dissipation rate at small enough scales $|\boldsymbol{r}|$. With this hypothesis, and with the approximation

$$\frac{\nu}{4}\overline{\frac{\partial u_i'^{+}}{\partial\zeta_k^{+}}\frac{\partial u_i'^{+}}{\partial\zeta_k^{+}}}+\frac{\nu}{4}\overline{\frac{\partial u_i'^{-}}{\partial\zeta_k^{-}}\frac{\partial u_i'^{-}}{\partial\zeta_k^{-}}}\approx\overline{\epsilon'}\tag{10.3}$$

which is acceptable at small enough $|\boldsymbol{r}|$, the small-scale turbulent energy balance (10.1) simplifies to

$$\boldsymbol{\nabla}_{\boldsymbol{r}}\cdot(\overline{\boldsymbol{\delta u'}|\boldsymbol{\delta u'}|^2})\approx-\overline{\epsilon'}\tag{10.4}$$

in an intermediate range of scales large enough to neglect viscous diffusion but small enough to neglect small-scale non-homogeneity. This balance incorporates the proportionality (8.24) but also sets the proportionality constant to -1. The similarity hypotheses required to obtain (8.24) are weaker than the local small-scale homogeneity hypothesis introduced here. *A priori*, they can be valid even if and when the local small-scale homogeneity hypothesis is not. When $\boldsymbol{\delta\bar{u}}$, P_r and P^s_{Xr} are negligible at small enough $|\boldsymbol{r}|$, as appears to be the case in the flow regions considered here, the local small-scale homogeneity hypothesis implies that the magnitude of $\boldsymbol{\nabla}_X\cdot(\overline{\boldsymbol{u}_{X'}\frac{1}{2}|\boldsymbol{\delta u'}|^2}+\overline{\boldsymbol{\delta u'}\delta p'})$ is increasingly small compared with $\overline{\epsilon'}$ with increasing Reynolds number for small

enough values of $|\boldsymbol{r}|$. It may be that, as the Reynolds number tends to infinity, (8.24) tends to (10.4) thereby recovering Kolmogorov's scale-by-scale equilibrium for homogeneous turbulence at small enough scales and implying that this Kolmogorov equilibrium is a very particular case of (8.24). However, it is not clear how such a statement could be established at the current time and in the foreseeable future.

We now use the kinematic relation (9.2), but we could also use its more general form (3.2) if we did not want to neglect $\boldsymbol{\delta\bar{u}}$, P_r and P^l_{Xr} from the outset. From (9.2) and (10.4) it follows that

$$\boldsymbol{\nabla}_{\boldsymbol{r}} \cdot \overline{\boldsymbol{\delta u'}|\boldsymbol{u}'_{\boldsymbol{X}}|^2} \approx \overline{\epsilon'} + 2\boldsymbol{\nabla}_{\boldsymbol{X}} \cdot (\overline{\boldsymbol{\delta u'}(\boldsymbol{\delta u'} \cdot \boldsymbol{u}'_{\boldsymbol{X}})}) \tag{10.5}$$

which is the analogue for stationary non-homogeneous turbulence of the Germano–Hosokawa relation (3.7) for homogeneous non-stationary (in fact freely decaying) turbulence.

Finally, the analogue of (3.8) for stationary non-homogeneous turbulence is obtained from (10.5) and (10.2) and it is

$$-P_X - P^l_{Xr} + \boldsymbol{\nabla}_{\boldsymbol{X}} \cdot \left(\overline{\boldsymbol{u}_{\boldsymbol{X}'} \tfrac{1}{2}|\boldsymbol{u}_{\boldsymbol{X}'}|^2} + \overline{\boldsymbol{u}_{\boldsymbol{X}'} p'_{\boldsymbol{X}}} + \overline{\boldsymbol{\delta u'}(\boldsymbol{\delta u'} \cdot \boldsymbol{u}'_{\boldsymbol{X}})} \right) \approx -\overline{\epsilon'}. \tag{10.6}$$

Like (10.4), equations (10.5) and (10.6) hold in an intermediate range of scales large enough to neglect viscous diffusion and small enough to neglect small-scale non-homogeneity. Note that (10.6) identifies a statistic characterising non-homogeneity which is proportional to $\overline{\epsilon'}$ with proportionality coefficient -1. This statistic is not captured by the non-equilibrium theory of non-homogeneous turbulence of § 8. In this case, the hypothesis of local small-scale homogeneity makes a prediction concerning turbulence non-homogeneity which is not accessible to the theory of § 8.

11. Conclusion

We have studied a turbulent flow region under rotating blades in a baffled container where the baffles break the rotation in the flow. The evidence from our 2D2C PIV supports the view that, within our PIV's field of view, two-point production makes a relatively small contribution to the small-scale energy equation (2.4) over a range of small two-point separation lengths. We assume the nonlinear and non-local dynamics of the small-scale turbulence to be effectively the same at different places. We have therefore made the similarity hypothesis that every term in the non-homogeneous but statistically stationary scale-by-scale (two-point) small-scale energy balance (6.1) has the same dependence on two-point separation at different positions $\boldsymbol{X}$ if rescaled by $\boldsymbol{X}$-local velocity and length scales. Following the theory of Chen & Vassilicos (2022) we have introduced such similarity hypotheses for both inner and outer scales and have considered intermediate matchings (see § 8). We have also improved the theory (i) by deriving the inner–outer equivalence hypothesis of Chen & Vassilicos (2022) for turbulence dissipation from a more intuitively natural hypothesis (see the last paragraph of § 8.3) and (ii) by taking explicit account of non-homogeneity in the inner to outer velocity ratios, thereby extending the theory's applicability range and removing the need for the theoretical adjustments in the Appendix of Chen & Vassilicos (2022) (see § 8 and in particular § 8.2).

This non-equilibrium theory of non-homogeneous small-scale turbulence predicts that an intermediate range of length scales exists where the interscale turbulence transfer rate, the two-point interspace turbulence transport rate and the two-point pressure gradient velocity correlation term in (6.1) are all proportional to the turbulence dissipation rate. Given the limitations of 2D2C PIV, we have been able to measure only parts (truncations)

of the interscale turbulence transfer rate and the two-point interspace turbulence transport rate in (6.1). This has forced us to introduce inner and outer hypotheses of isotropic similarity applicable to the truncations accessible to our measurements. With these hypotheses (which should not be confused with hypotheses of isotropy) the theory leads to the same predictions for the 2D2C PIV-truncated interscale turbulence transfer rate and two-point interspace turbulence transport rate in (6.1). Our 2D2C PIV measurements suggest that these truncations may indeed be independent of two-point separation scale and be proportional to the average turbulence dissipation rate over a more or less overlapping range of scales as predicted by the theory. The PIV-truncated two-point interspace turbulence transport rate is significantly non-zero, thereby reflecting both the presence of small-scale non-homogeneity and the absence of Kolmogorov scale-by-scale equilibrium. Its proportionality with the turbulence dissipation rate is evidence that small-scale non-homogeneity and non-equilibrium do actually obey general rules.

The PIV-truncated average interscale transfer rate of small-scale turbulent energy is negative, suggesting forward cascade if the corresponding full (non-truncated) average interscale transfer rate has the same sign, and the PIV-truncated average interspace turbulent transfer rate of small-scale turbulence energy is positive, suggesting outward turbulent transport of small-scale turbulence if the corresponding full (non-truncated) average interspace turbulent transfer rate is also positive.

We have also applied hypotheses of inner and outer similarity as well as inner and outer isotropic similarity to second-order structure functions of turbulent fluctuating velocities. Inner–outer intermediate matching has led to the prediction of power-law dependencies on turbulence dissipation rate and two-point separation length with power-law exponent $n = 2/3$. The 2D2C PIV has provided support for this Kolmogorov-like value of the exponent in the r_x direction but not in the r_z direction where the PIV suggests an exponent n between 0.5 and 0.6. Future studies should investigate whether rotation, even if effectively faint within our field of view because of the rotation-breaking effect of the baffles, may require similarity forms in terms of more than one outer length scale l_O and more than one inner length scale l_I, depending on direction. The value of the exponent n impacts only the Reynolds-number dependencies of l_I/l_O and V_I/V_O and has no direct impact on the other predictions of the theory. The exponent $n = 2/3$ implies the Kolmogorov-like scalings (8.19) and (8.20).

The large-scale turbulent energy budget (2.8) is very different from the small-scale turbulent energy budget (2.4) in terms of both production and interspace turbulence transport which are both non-zero in the limit of zero two-point separation lengths when the turbulence is inhomogeneous. We have therefore not applied to (2.8) the similarity approach that we applied to (2.4). However, we have taken advantage of the kinematic relation which exists between the rate with which large scales gain or lose turbulent energy to the small scales via nonlinear turbulence interactions (present in (2.8)) and the rate with which small scales gain or lose turbulent energy via such interactions (present in (2.4)). The PIV-truncated part of the rate with which large scales gain or lose turbulent energy to the small scales has turned out to be approximately independent of two-point separation scale and proportional to the average turbulence dissipation rate over the same range of scales where the PIV-truncated interscale transfer rate in (2.4)) exhibits the same behaviour. However, these two transfer rates do not balance, which suggests that the transfer of turbulent energy from large to small scales (or vice versa) may not be 'impermeable' in the sense that energy may be leaking out of this cascade process because of non-homogeneities, in the present case by the spatial gradient term on the right-hand side of (9.2).

Our non-equilibrium theory of non-homogeneous turbulence does not give the proportionality coefficients in (8.23), (8.24) and (8.25). We have therefore introduced a local small-scale homogeneity hypothesis in § 10 as a space analogue of Kolmogorov's small-scale stationarity hypothesis but do not have criteria, at this stage, for the validity of this small-scale homogeneity hypothesis. If and when this new hypothesis may hold (perhaps in the limit of infinite Reynolds numbers?) the coefficient of proportionality in (8.24) will be -1.

Supplementary material. Supplementary material is available at https://doi.org/10.1017/jfm.2024.220.

Acknowledgements. The CNRS Research Federation on Ground Transports and Mobility, in articulation with the Elsat2020 project supported by the European Community, the French Ministry of Higher Education and Research, the Hauts de France Regional Council are acknowledged for the funding of the PIV equipment used in this study. We thank J.-P. Laval for providing the direct numerical simulation data used in § 3 of the supplementary material.

Funding. This work was directly supported by JCV's Chair of Excellence CoPreFlo funded by I-SITE-ULNE (grant number R-TALENT-19-001-VASSILICOS), MEL (grant number CONVENTION_219_ESR_06) and Region Hauts de France (grant number 20003862). Funded by the European Union (ERC, NoStaHo, 101054117). Views and opinions expressed are, however, those of the author(s) only and do not necessarily reflect those of the European Union or the European Research Council. Neither the European Union nor the granting authority can be held responsible for them.

Declaration of interests. The authors report no conflict of interest.

Data availability statement. The data that support the findings of this study are available upon request.

Author ORCIDs.
P. Beaumard https://orcid.org/0009-0003-6654-1854;
P. Bragança https://orcid.org/0009-0005-5290-1913;
C. Cuvier https://orcid.org/0000-0001-6108-6942;
K. Steiros https://orcid.org/0000-0001-7779-170X;
J.C. Vassilicos https://orcid.org/0000-0003-1828-6628.

Appendix A. Individual contributions of interspace and interscale energy transfer rate

In § 8.4, the truncated estimates of the interscale transfer rate

$$\frac{\partial}{\partial r_x}\langle\overline{[\delta u_x'(\delta u_x'^2+\delta u_z'^2)]}\rangle/\langle\overline{\epsilon'}\rangle+\frac{\partial}{\partial r_z}\langle\overline{[\delta u_z'(\delta u_x'^2+\delta u_z'^2)]}\rangle/\langle\overline{\epsilon'}\rangle \tag{A1}$$

are found to exhibit a significant range of scales where they are approximately constant with r_x and r_z and to also collapse acceptably well for the different experimental configurations. One can also analyse subterms of the part of the average interscale transfer rate that we measure. In figure 15, we plot

$$\frac{\partial}{\partial r_x}\langle\overline{[\delta u_x'(\delta u_x'^2+\delta u_z'^2)]}\rangle/\langle\overline{\epsilon'}\rangle \quad \text{and} \quad \frac{\partial}{\partial r_z}\langle\overline{[\delta u_z'(\delta u_x'^2+\delta u_z'^2)]}\rangle/\langle\overline{\epsilon'}\rangle \tag{A2a,b}$$

separately and see that they are both constant over the range of scales where their sum is constant and that they both contribute significantly to that sum but that the latter is also significantly larger in magnitude than the former.

The same analysis is done for the truncated estimates of the interspace transfer rate which is also found in § 8.4 to collapse for different experimental configurations and to be

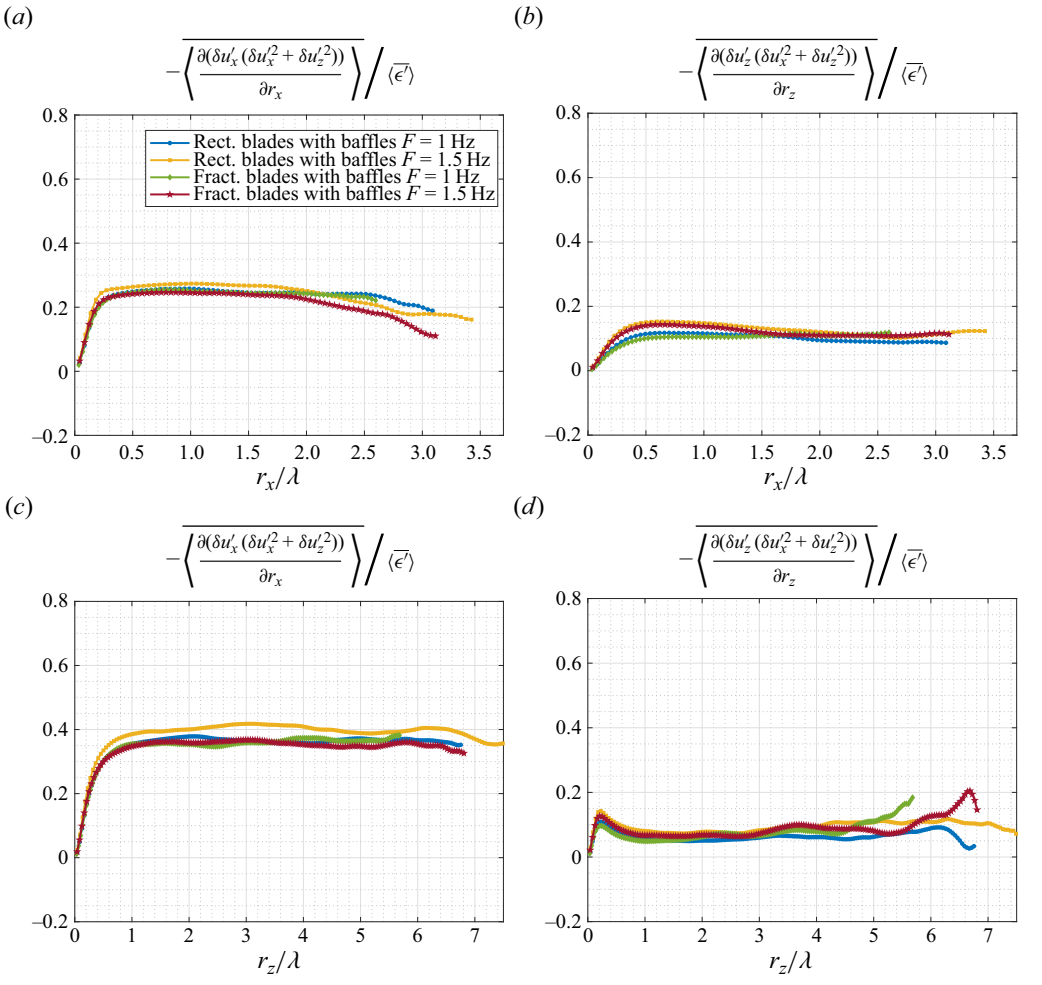

Figure 15. Interscale transfer rate. (*a*) Interscale transfer rate ∂/r_x contribution in r_x direction. (*b*) Interscale transfer rate ∂/r_z contribution estimate in r_x direction. (*c*) Interscale transfer rate ∂/r_x contribution estimate in r_z direction. (*d*) Interscale transfer rate ∂/r_z contribution estimate in r_z direction.

approximately constant over a significant range of scales r_x and r_z. In figure 16, we plot

$$\frac{\partial}{\partial X_x}\langle\overline{[u'_{Xx}(\delta u_x'^2+\delta u_z'^2)]}\rangle/\langle\overline{\epsilon'}\rangle \quad \text{and} \quad \frac{\partial}{\partial X_z}\langle\overline{[u'_{Xz}(\delta u_x'^2+\delta u_z'^2)]}\rangle/\langle\overline{\epsilon'}\rangle \tag{A3a,b}$$

separately and we report an acceptable collapse for different experimental configurations and an approximate constancy in r_x and r_z over the range of scales where their sum is constant. We note, however, a decreasing dependence on r_x of

$$\frac{\partial}{\partial X_x}\langle\overline{[u'_{Xx}(\delta u_x'^2+\delta u_z'^2)]}\rangle/\langle\overline{\epsilon'}\rangle \tag{A4}$$

for the rectangular blade $F = 1$ Hz configuration. This outlier might be associated with statistical convergence uncertainty and/or deviations from the theory's predictions in this particular configuration which combines lower Reynolds number with slower mixing because of larger large-scale coherent structures.

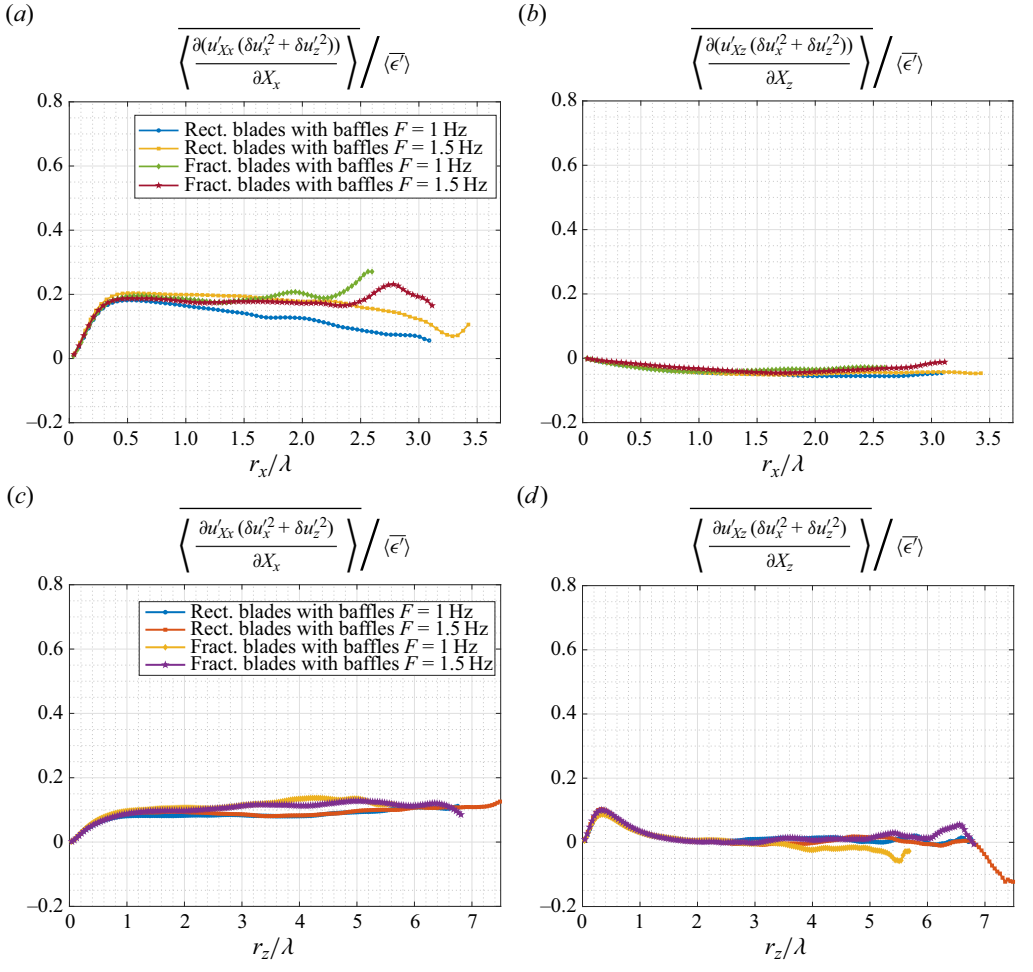

Figure 16. Interspace transport rate. (*a*) Interspace transport rate ∂/X_x contribution in r_x direction. (*b*) Interspace transport rate ∂/X_z contribution estimate in r_x direction. (*c*) Interspace transport rate ∂/X_x contribution estimate in r_z direction. (*d*) Interspace transport rate ∂/X_z contribution estimate in r_z direction.

References

Alexakis, A. 2023 How far does turbulence spread? *J. Fluid Mech.* **977**, R1.

Alves Portela, F., Papadakis, G. & Vassilicos, J.C. 2017 The turbulence cascade in the near wake of a square prism. *J. Fluid Mech.* **825**, 315–352.

Alves Portela, F., Papadakis, G. & Vassilicos, J.C. 2020 The role of coherent structures and inhomogeneity in near-field inter-scale turbulent energy transfers. *J. Fluid Mech.* **896**, A16.

Apostolidis, A, Laval, J.P. & Vassilicos, J.C. 2023 Turbulent cascade in fully developed 2 turbulent channel flow. *J. Fluid Mech.* **967**, A22.

Baroud, C.N., Plapp, B.B., She, Z.-S. & Swinney, H.L. 2002 Anomalous self-similarity in a turbulent rapidly rotating fluid. *Phys. Rev. Lett.* **88** (11), 114501.

Chen, J.G. & Vassilicos, J.C. 2022 Scalings of scale-by-scale turbulence energy in non-homogeneous turbulence. *J. Fluid Mech.* **938**, A7.

Christensen, K.T. 2004 The influence of peak-locking errors on turbulence statistics computed from PIV ensembles. *Exp. Fluids* **36** (3), 484–497.

Foucaut, J.M., George, W.K., Stanislas, M. & Cuvier, C. 2021 Optimization of a SPIV experiment for derivative moments assessment in a turbulent boundary layer. *Exp. Fluids* **62** (12), 244.

Frisch, U. 1995 *Turbulence: The Legacy of A. N. Kolmogorov*. Cambridge University Press.

GERMANO, M. 2007 The elementary energy transfer between the two-point velocity mean and difference. *Phys. Fluids* **19** (8), 085105.

HILL, R.J. 2001 Equations relating structure functions of all orders. *J. Fluid Mech.* **434**, 379–388.

HILL, R.J. 2002 The approach of turbulence to the locally homogeneous asymptote as studied using exact structure-function equations. arXiv:physics/0206034.

HOSOKAWA, I. 2007 A paradox concerning the refined similarity hypothesis of Kolmogorov for isotropic turbulence. *Prog. Theor. Phys.* **118** (1), 169–173.

KEANE, R.D. & ADRIAN, R.J. 1991 Optimization of particle image velocimeters: II. Multiple pulsed systems. *Meas. Sci. Technol.* **2** (10), 963–974.

LAIZET, S., NEDIĆ, J. & VASSILICOS, J.C. 2015 Influence of the spatial resolution on fine-scale features in DNS of turbulence generated by a single square grid. *Intl J. Comput. Fluid Dyn.* **29** (3–5), 286–302.

LARSSEN, H.S. & VASSILICOS, J.C. 2023 Spatio-temporal fluctuations of interscale and interspace energy transfer dynamics in homogeneous turbulence. *J. Fluid Mech.* **969**, A14.

LAVOIE, P., AVALLONE, G., DE GREGORIO, F., ROMANO, G.P. & ANTONIA, R.A. 2007 Spatial resolution of PIV for the measurement of turbulence. *Exp. Fluids* **43** (1), 39–51.

LECORDIER, B. & TRINITÉ, M. 2004 Advanced PIV algorithms with image distortion validation and comparison using synthetic images of turbulent flow. In *Particle Image Velocimetry: Recent Improvements* (ed. M. Stanislas, J. Westerweel & J. Kompenhans), pp. 115–132. Springer.

MELDI, M. & VASSILICOS, J.C. 2021 Analysis of Lundgren's matched asymptotic expansion approach to the Kármán–Howarth equation using the eddy damped quasinormal Markovian turbulence closure. *Phys. Rev. Fluids* **6** (6), 064602.

NAGATA, S. 1975 Mixing: principles and applications. John Wiley & Sons, Halstead Press.

OBLIGADO, M. & VASSILICOS, J.C. 2019 The non-equilibrium part of the inertial range in decaying homogeneous turbulence. *Europhys. Lett.* **127** (6), 64004.

POPE, S.B. 2000 *Turbulent Flows*. Cambridge University Press.

RAFFEL, M., WILLERT, C.E., SCARANO, F., KÄHLER, C.J., WERELEY, S.T. & KOMPENHANS, J. 2018 *Particle Image Velocimetry: A Practical Guide*. Springer International Publishing.

SCARANO, F. 2001 Iterative image deformation methods in PIV. *Meas. Sci. Technol.* **13**, R1.

SORIA, J. 1996 An investigation of the near wake of a circular cylinder using a video-based digital cross-correlation particle image velocimetry technique. *Exp. Therm. Fluid Sci.* **12** (2), 221–233.

STEIROS, K., BRUCE, P.J.K., BUXTON, O.R.H. & VASSILICOS, J.C. 2017*a* Effect of blade modifications on the torque and flow field of radial impellers in stirred tanks. *Phys. Rev. Fluids* **2** (9), 094802.

STEIROS, K., BRUCE, P.J.K., BUXTON, O.R.H. & VASSILICOS, J.C. 2017*b* Power consumption and form drag of regular and fractal-shaped turbines in a stirred tank. *AIChE J.* **63** (2), 843–854.

TENNEKES, H. & LUMLEY, J.L. 1972 *A First Course in Turbulence*. MIT.

WILLERT, C.E. & GHARIB, M. 1991 Digital particle image velocimetry. *Exp. Fluids* **10** (4), 181–193.

ZHOU, Y. & VASSILICOS, J.C. 2020 Energy cascade at the turbulent/nonturbulent interface. *Phys. Rev. Fluids* **5** (6), 064604.